

X-RAY REPROCESSING: THROUGH THE ECLIPSE SPECTRA OF HIGH MASS X-RAY BINARIES WITH *XMM-NEWTON*

NAFISA AFTAB¹, BISWAJIT PAUL¹, AND PETER KRETSCHMAR²

¹Raman Research Institute, C V Raman Avenue, Sadashivanagar, Bangalore 560080, India and

²European Space Agency European Space Astronomy Center (ESA-ESAC), amino Bajo del Castillo, s/n., Urb. Villafranca del Castillo, 28692 Villanueva de la Canada, Madrid, Spain

Draft version June 20, 2019

ABSTRACT

The study of X-ray reprocessing is one of the key diagnostic tools to probe the environment in X-ray binary systems. One difficult aspect of studying X-ray reprocessing is the presence of much brighter primary radiation from the compact star together with the reprocessed radiation. In contrast for eclipsing systems, the X-rays we receive during eclipse are only those produced by reprocessing of the emission from the compact star by the surrounding medium. We report results from a spectral study of the X-ray emission during eclipse and outside eclipse (when available) in 9 high mass X-ray binaries (HMXBs) with *XMM-Newton* EPIC pn to investigate different aspects of the stellar wind in these HMXBs. During eclipse the continuum component of the spectrum is reduced by a factor of ~ 8 –237, but the count-rate for 6.4 keV Iron emission line or complex of Iron emission lines in HMXBs are reduced by a smaller factor leading to large equivalent widths of the Iron emission lines. This indicates a large size for the line emission region, comparable to or larger than the companion star in these HMXB systems. However there are significant system to system differences. 4U 1538–52, in spite of having a large absorption column density, shows a soft emission component with comparable flux during the eclipse and out-of-eclipse phases. Emission from Hydrogen-like Iron has been observed in LMC X-4 for the first time, in the out-of-eclipse phase in one of the observations. Overall, we find significant differences in the eclipse spectrum of different HMXBs and also in their eclipse spectra against out-of-eclipse spectra.

Keywords: (stars:) binaries: eclipsing – stars: neutron – (stars:) supergiants

1. INTRODUCTION

In X-ray binary systems, the X-rays produced very close to the compact object fuelled by accretion are called primary X-rays. Usually a large part of these X-rays escapes directly from the system and can be directly observed. But a significant fraction interacts with the matter surrounding the compact object and are re-emitted. This emission is called secondary emission. Depending upon the interaction of the primary X-rays with the surrounding matter, the secondary photons can have a wide range of energies. This phenomenon is known as reprocessing of X-rays (or X-ray reprocessing). The secondary emission as a whole is called reprocessed emission and the secondary X-rays are known as reprocessed X-rays.

Low energy primary X-rays colliding with very low energy electrons through Thomson scattering are reflected with the same energy as they had before the interaction. Higher energy X-rays can interact with lower energy electrons, giving off some of their energy to the electrons via Compton scattering and coming out as lower energy X-rays, UV, or optical photons. Moderate energy X-rays can be upscattered by relativistic electrons of the hot plasma and gain energy. Some X-rays interact with ionized or neutral atoms, excite electrons and give rise to different spectral lines in the X-ray, UV, or optical bands. X-ray photons can be absorbed by photoionization of neutral or ionized atoms leading to reemission of photons at lower energies. Photons can also be affected by gravitational redshift. Reprocessing of X-rays is ubiquitous and has been observed in systems with accreting black holes, neutron stars, white dwarfs and in active galactic nuclei (AGN).

The X-ray reprocessing characteristics as seen from the Earth depend upon several factors, for example 1) density and distribution of matter around the accretor; 2) structures in an accretion disc, if one is present 3) the orbital phase of the system; 4) the chemical composition and ionization levels of the matter in the system; 5) the viewing angle of the observer. Studying X-ray reprocessing has been proven to be a very useful tool to unveil the geometry, distribution of matter and its ionization level and also accretion mechanisms of accreting systems.

There have been theoretical and observational studies on X-ray reprocessing starting from AGNs to low mass X-ray binary (LMXB) systems, which have revealed different unique features of these systems, for example: AGN – Zycki et al. (1994); LMXB – de Jong, van Paradijs & Augusteijn (1996); Seyfert galaxy NGC 2992 – Weaver et al. (1996); supersoft X-ray source (SSS) CAL 87 (cataclysmic variable) – Suleimanov, Meyer & Meyer-Hofmeister (2003); black hole binary XTE J1817–330 – Gierliński, Done & Page (2009) etc.

In this work we focus on the X-ray reprocessing in high mass X-ray binary (HMXB) systems. In HMXB systems the companion star is a high mass star ($\geq 10M_{\odot}$), either a main-sequence star or a supergiant and the compact object is either a neutron star or a black hole. In HMXB systems with a supergiant companion (SgHMXB system) most of the time the compact object is embedded in the dense wind of the companion star, so the primary X-rays encounter scattering in these systems which results into reprocessing. Often the supergiant’s wind contains clumps of different densities and sizes and intra-clump regions are filled with rarefied wind materials (Oskinson, Feldmeier & Kretschmar 2013). The reverse scenario is also possible,

i.e., there could be lower density zones in a dense ambient medium. This causes variation of X-ray reprocessing with the distribution of matter around the compact object. Supergiant fast X-ray transients (SFXTs) are a newer class of SgHMXBs (Negueruela et al. 2006; Sguera et al. 2005) which are usually dim sources (average luminosity 10^{33} - 10^{34} erg s $^{-1}$), but often appear with unpredicted intense flares (flare luminosity reaches 10^{36} - 10^{37} erg s $^{-1}$). However, most of the time the SFXTs have X-ray luminosity that is 3-4 orders of magnitude fainter compared to the classical HMXBs. (luminosity at quiescent 10^{32} erg s $^{-1}$). These drastic change of luminosities in SFXTs indicates quite dynamic accretion scenario in these systems, hence variable wind structures around the compact object or different interaction between the compact object and companion's wind. In both the cases large variation in X-ray reprocessing is expected. Accretion discs exist in some HMXB systems (Cen X-3, LMC X-4, SMC X-1: Savonije 1978; van der Meer et al. 2007). Frequently structures (warps) form and decay in the accretion disc. The structures can differ in density, temperature, shape etc. and face different solid angle to the primary X-rays. Moreover these structures evolve with time, causing variation in the X-ray reprocessing.

Analyzing reprocessed X-ray emissions we can derive clues about the environment of the compact object in an X-ray binary system. But the difficult aspect of studying reprocessed X-rays in X-ray binary systems is that the reprocessed emission is detected along with the primary emission from the compact object, which is much brighter. During eclipse the primary X-rays are blocked by the companion and the X-rays we receive are the reprocessed X-rays only. The intensity of the reprocessed X-rays is expected to be smaller by a factor of a few. This increases the equivalent width of a spectral line, when the emitting material is distributed in an extended region. Thus the detection of a spectral line becomes more significant during eclipse. These spectral lines give useful informations about the chemical composition and ionization state of matter around the compact object. When the compact object is not in eclipse, then the line intensity may be less significant compared to the continuum and therefore difficult to measure accurately (if the line intensity itself is not very intense). This results into low equivalent width and the line detection becomes less significant during out-of-eclipse. The comparison of equivalent width during eclipse can give useful insight about the distribution of different matter in different binary systems and in a binary system at different epochs, in much more efficient way compared to the out-of-eclipse phase.

Eclipse spectra of individual sources have been reported before (Cen X-3 – Naik & Paul 2012; Wojdowski, Liedahl & Sako 2001; Ebisawa et al. 1996, 4U 1538–522 – Rodes-Roca et al. 2011, 4U 1700–377 – van der Meer et al. 2005a, Vela X-1 – Sako et al. 1999; Schulz et al. 2002). The scattered reports on individual sources do not give an overall picture of the extent of reprocessing during eclipse in HMXBs, i.e., what is the fractional luminosity compared to the out-of-eclipse spectrum, how do the shape of the continuum during the eclipse compare with the out-of-eclipse spectrum, relative strength of the Iron (Fe) fluorescence line and other Fe lines if present. Moreover, we also aim to study system to system variability, possible dependences on the type, mass, or mass loss rate of the companion and also to investigate the stability of the reprocessing in a given source when multiple data sets exist. There in-

deed exist a large number of papers that investigate or use reprocessing as a tool, but this is the first work on a comprehensive analysis of all eclipse data available of HMXB systems with *XMM-Newton* EPIC pn, an instrument particularly suitable for its large collection area and CCD spectral resolution for the study of isolated emission lines.

Out of 15 eclipsing HMXBs 9 sources have been observed with *XMM-Newton*. In this work we have analyzed all available observations of the HMXBs with *XMM-Newton* EPIC pn that include eclipses, i.e in 7 Supergiant HMXBs or SgHMXBs (Cen X-3, 4U 1700–377, 4U 1538–52, SMC X-1, LMC X-4, IGR J18027–2016, IGR J17252–3616) and in 2 Supergiant Fast X-ray Transients (SFXTs) namely IGR J16479–4514 and IGR J16418–4532. We have focussed on these observations in order to have a coherent sample of data for analysis and comparison. A list of the important parameters of these sources are given in Table 1. In the following paragraph we discuss some of the observed features of these systems which are relevant to our analysis.

Cen X-3 was the first discovered X-ray binary pulsar (Giacconi et al. 1971) which accretes matter directly from the supergiant's wind and also through disk accretion via Roche Lobe overflow (Nagase et al. 1992; Day & Stevens 1993). Nagase et al. (1992) observed an Fe line in Cen X-3 with energy ~ 6.5 keV. The intensity of this line was observed to be pulsating with phase, which indicates that the matter surrounding the neutron star causing this fluorescent line is not uniformly distributed (Day & Stevens 1993). Ebisawa et al. (1996) with 1993 ASCA observation have clearly resolved three Fe K_{α} emission lines with energy of 6.4 keV, 6.7 keV and 6.97 keV during eclipse. The highly ionized 6.7 keV and 6.97 keV emission lines could not be resolved in the pre eclipse phase. The line parameters indicate that the origin of the fluorescent 6.4 keV was nearer to the neutron star as compared to that of the highly ionized Fe K_{α} emission lines. del Sordo et al. (2000) have investigated two BeppoSAX observations of Cen X-3 in August 1996 and in February 1997. They found significantly higher energy of the fluorescent Fe K_{α} emission line (~ 6.6 keV), which could be a blend of 6.4 keV emission line with 6.7 keV emission line originating from hot matter surrounding the neutron star. Naik & Paul (2012) with the same *XMM-Newton* observation which we have analysed here, found significant variability in the line parameters of the three Fe K_{α} emission lines during eclipse and out-of-eclipse phases. They also suggest that the colder material, causing 6.4 keV line emission, is relatively close to the neutron star at most on the scale of the companion, while the hot matter producing the Fe XXV and Fe XXVI emission lines are further away as suggested by Ebisawa et al. (1996). A cyclotron resonance scattering feature at 28 keV and 30 keV has been detected in Cen X-3 with two *BeppoSAX* observations (Santangelo et al. 1998; Burderi et al. 2000). *Suzaku* observation of Cen X-3 covering a full binary orbit showed multiple extended dips with spectral characteristics similar to that of the source in eclipse, indicating the dips to be produced due to obscuration by dense matter which are structures in the outer region of the accretion disk (Naik, Paul & Ali 2011).

LMC X-4 is a wind and disk fed persistent system in the Large Magellanic Cloud (LMC) which often shows X-ray flares sometimes with super Eddington luminosity (Levine, Rappaport & Zojcheski 2000; Moon, Eikenberry & Wasserman 2003). The source was found to show pe-

Table 1

List of basic parameters of the eclipsing HMXBs analyzed in this work, where P_{orb} : Orbital Period (days), M_C : Mass of the companion (M_{\odot}), R_C : Radius of the companion star (R_{\odot}), S_C : Spectral type of the companion, e : Eccentricity of the HMXB orbit, a : Length of the semi major axis of the system ($a_x \sin i$ [light-sec]), \dot{M}_w : Mass loss of the companion star ($10^{-7} M_{\odot} \text{ yr}^{-1}$), d : Distance from Earth (kpc). (M_{\odot} , R_{\odot} : Mass and radius of Sun respectively)

Source	Mode of accretion	P_{orb}	M_C	R_C	S_C	e	a	\dot{M}_w	d
Cen X-3	wind+disc ^{a1}	2.09 ^{a2}	(20.5±0.7) ^{a3}	12.1± 0.5 ^{a4}	O6.5 II-III ^{a4}	≤0.0016 ^{a5}	39.6612±0.0009 ^{a6}	5.3 ^{a1}	5.7±1.5 ^{a7}
LMC X-4	wind+disc ^{a1}	1.41 ^{b2}	14.5 ^{+1.1} _{-1.0} ^{a4}	7.8 ^{+0.3} _{-0.4} ^{a4}	O8 III ^{a4}	0.0006±0.0002 ^{b3}	26.343±0.016 ^{b3}	2.4 ^{a1}	49.97±0.19±1.11 ^{b4}
SMC X-1	wind+disc ^{a1}	3.89 ^{c2}	(16.6 ± 0.4) ^{c3}	18 ^{c4}	B0 I ^{c5}	<0.0007 ^{c4}	53.4876 lt-sec ^{c6}	15 ^{a1}	60.6±1.0±2.8 ^{c7}
4U 1700–377	wind ^{a1}	3.412 ^{d1}	(52 ± 2) ^{d2}	21.9 ^{+1.3} _{-0.5} ^{d2}	O7f ^{d3}	<0.008 ^{d4}	48-82 ^{d1}	>21 ^{a1}	1.8 ^{d5}
4U 1538–522	wind ^{a1}	3.75 ^{e2}	(19.9±3.4) ^{e3}	17.2±1.0 ^{e3}	B0Iab ^{e4}	0.174±0.015 ^{e5}	53.1±1.5 ^{e5}	8.3 ^{a1}	6.4±1.0 ^{e5}
IGR J18027–2016	wind ^{a1}	4.56 ^{f2}	18.8–29.3 ^{f2}	(15.0–23.4) ^{f2}	B1-Ib ^{f3}	6.3 ^{f1b}	68±1 ^{f2}	6.3 ^{a1}	-
IGR J17252–3616	wind ^{a1}	9.74 ⁱ²	15 ⁱ³	21–37 ⁱ²	B0 I–B5 I ⁱ²	<0.19 ⁱ²	101±3 ⁱ²	9.0 ^{a1}	5.3-8.7 ⁱ²
IGR J16479–4514	SFXT ^{g0} , ^{g1}	3.32 ^{g2}	30 ^{g3}	23.8 ^{g3}	O9.5 Iab ^{g4}	-	(44.85-48.90) ^{z1}	(10-70) ^{y2}	2.8 ^{+4.9} _{-1.7} ^{g4}
IGR J16418–4532	SFXT ^{h0}	3.75 ^{h2}	31.54 ^{h3}	21.41 ^{h3}	BN 0.5 Ia ^{h4}	-	(48.65-53.03) ^{z2}	(2.3-3.8) ^{y3}	13 ^{h5}

^{a1}(Falanga et al. 2015), ^{a2}(Schreier et al. 1972b), ^{a3}(Ash et al. 1999), ^{a4}(van der Meer et al. 2007), ^{a5}(Bildsten et al. 1997), ^{a6}(Raichur & Paul 2010), ^{a7}(Thompson & Rothschild 2009),

^{b2}(Li, Rappaport & Epstein 1978); (White 1978), ^{b3}(Levine, Rappaport & Zojcheski 2000), ^{b4}(Pietrzyński et al. 2013),

^{c2}(Schreier et al. 1972a), ^{c3}(Val Baker, Norton & Quaintrell 2005), ^{c4}(Primini, Rappaport & Joss 1977), ^{c5}(Reynolds et al. 1993), ^{c6}(Levine et al. 1993), ^{c7}(Hilditch, Howarth & Harries 2005)

^{d1}(Jones et al. 1973), ^{d2}(Clark et al. 2002), ^{d3}(Penny et al. 1973), ^{d4}(Islam & Paul 2016), ^{d5}(Ankay et al. 2001)

^{e2}(Becker et al. 1977), ^{e3}(Reynolds, Bell & Hilditch 1992), ^{e4}(Parkes, Murdin & Mason 1978), (Falanga et al. 2015), ^{e5}(Mukherjee et al. 2006),

^{f1b}(Augello et al. 2003), ^{f2}(Hill et al. 2005), (Jain, Paul & Dutta 2009b), ^{f3}(Torrejón et al. 2010),

^{g0}(Sguera et al. 2005), ^{g1}(Molkov et al. 2003), ^{g2}(Jain, Paul & Dutta 2009a), ^{g3}(Vacca, Garmany & Shull 1996), ^{g4}(Nespoli, Fabregat & Mennickent 2008),

^{h0}(Romano et al. 2011), ^{h2}(Corbet et al. 2006), ^{h3}(Martins, Schaerer & Hillier 2005), ^{h4}(Coleiro et al. 2013),

ⁱ²(Thompson et al. 2007), ⁱ³(Takeuchi, Koyama & Warwick 1990)

^{y2}(Sidoli et al. 2012a), ^{y3}(Drave et al. 2013b)

^{z1}, ^{z2} Derived from total mass of the binary and the orbital period, taken from Coley, Corbet & Krimm (2015)

riodicity longer than the orbital period known as super-orbital period of 30.5 days (Lang et al. 1981). The pulsation of the soft spectral component and the powerlaw component showed significant phase differences with the *ROSAT*, *GINGA*, *ASCA*, *BeppoSAX* and *XMM-Newton* and *Suzaku* observatories (Woo et al. 1996; Paul & Kitamoto 2002; Naik & Paul 2004b; Beri & Paul 2017; Hung et al. 2010). These indicate different origin of the soft and hard X-rays. LMC X-4 shows short super-Eddington bursts, during which the pulse profile of the pulsar changes both in phase and shape. Same has been observed with *RXTE-PCA* (Levine, Rappaport & Zojchowski 2000), *XMM-Newton* (Beri & Paul 2017) and *NuStar* (Shtykovsky et al. 2018).

SMC X-1 is a wind and disk fed binary pulsar located in the Small Magellanic Cloud (SMC), which has been observed with both at sub-Eddington and super-Eddington luminosities and shows short and intense bursts like LMC X-4 (Price et al. 1971; Ulmer et al. 1973; Coe et al. 1981). It has a highly variable superorbital period (between ~ 40 -65 days, Hu et al. 2013). *ROSAT*, *GINGA* and *ASCA* observations of the source show out-of-eclipse flux variation by a factor of 20 between high and low state while eclipsed flux and spectral parameters remain nearly same in both the states. This possibly indicates blocking of the neutron star's direct emission by a precessing tilted accretion disk (Wojdowski et al. 1998). Observations of SMC X-1 have been carried out at different superorbital phases with *Chandra* and *XMM-Newton* to investigate the case of a precessing warped accretion disk in this source (Hickox & Vrtilek 2005). Broadband spectroscopy of SMC X-1 carried out with multiple *Suzaku* (Kubota et al. 2018) and *NuStar* (Pike et al. 2019) observations have reinforced the same.

4U 1700–377 is a high mass X-ray binary wind fed system in which the nature of the compact object is not yet clear. The source has been observed with pronounced variability with strong flares, which is believed to be due to accretion from the supergiant's inhomogeneous wind (White, Kallman & Swank 1983). van der Meer et al. (2005b) have detected several recombination and fluorescent lines including highly ionized and fluorescent Fe K_{α} emission lines in the eclipse and eclipse egress and low flux *XMM-Newton* spectra, where lines are most prominent during eclipse. They suggest extended ionized plasma surrounding the compact object. Jaisawal & Naik (2015) have found 6.4 keV Fe K_{α} and 7.1 keV Fe K_{β} emission lines in 20 time resolved out-of-eclipse *Suzaku* spectra of the source. The relation between the flux and equivalent width of these Fe emission lines indicate that these lines originate from the matter near the compact object. They found a significant increase of the line of sight equivalent Hydrogen column density during low flux out-of-eclipse phases, indicating an inhomogeneous distribution of the wind.

4U 1538–522 is a wind fed X-ray binary pulsar. Rodes-Roca et al. (2011) have analyzed eclipse and phase averaged out-of-eclipse spectra with *XMM-Newton*. They found Fe emission lines in the energy range of 6–7 keV and several recombination lines below 3 keV in the eclipse spectrum. These indicate presence of emitting material over a large distance comparable or greater than the size of the supergiant companion. Mukherjee et al. (2006) have detected a 6.4 keV Fe emission line with *RXTE* and *BeppoSAX*. They have found varying line of sight equivalent Hydrogen column density over the orbital phase which increases before and after the eclipse asymmetrically. This

indicates a trailing accretion stream or wakes from the supergiant companion. A cyclotron resonance scattering feature at around 22 keV has been observed in 4U 1538–52 in detail with *Suzaku* (Hemphill et al. 2014), *AstroSat* (Varun et al. 2019) and *NuStar* (Hemphill et al. 2019).

IGR J18027–2016 is a wind fed high-mass X-ray binary pulsar. *INTEGRAL* and *XMM-Newton* observations of the source show a high value of the line of sight Hydrogen column density, which indicates intrinsic absorption (Hill et al. 2005). Aftab, Islam & Paul (2016) have found several low intensity states in the source with *Swift-XRT*, while *Swift-BAT* shows smooth variation over the orbit. They have also found high value of line of sight Hydrogen column density, which even increases more before and after the eclipse. These indicate an accreting trailing wind from the supergiant companion to the pulsar crossing the line of sight like in 4U 1538–522. A cyclotron resonance scattering feature at 23 keV has been discovered in IGR J18027–2016 with *NuStar* (Lutovinov et al. 2017).

IGR J17252–3616 is a wind fed X-ray binary pulsar showing strong X-ray absorption (Walter et al. 2004; Tawara et al. 1989). Thompson et al. (2007) have obtained orbital phase resolved spectroscopy with *RXTE*. They have found variation in flux, line of sight equivalent Hydrogen column density, photon index and Fe line equivalent width. Column densities rise by a factor of ≥ 10 just before the eclipse ingress and after the egress, this indicates spherically symmetric wind outflow from the supergiant which is trailing the pulsar in its orbit.

IGR J16479–4514 and IGR J16418–4532 are SFXTs discovered with *INTEGRAL* in 2003 (Negueruela et al. 2006; Sguera et al. 2005). IGR J16479–4514 showed more frequent X-ray outburst than other SFXTs in the past (Walter & Zurita Heras 2007). It is the SFXT with smallest orbital period of 3.32 days (Jain, Paul & Dutta 2009a). Accretion onto the compact object is very likely from the supergiant's wind (Romano et al. 2008). The X-ray emission from the source was observed to be highly variable on time-scales of seconds to weeks during outbursts and in quiescence (Sidoli et al. 2008). Occurrence of flares in similar orbital phases, suggests phase locked wind structure in the system (Bozzo et al. 2009; Sidoli et al. 2013). IGR J16418–4532 is a heavily absorbed pulsar as observed with *INTEGRAL* (Walter et al. 2006). A superorbital modulation has been observed in the source (Corbet & Krimm 2013; Drave et al. 2013a). It is an intermediate accretor between pure wind accretion and full Roche lobe overflow (Sidoli et al. 2012b). Drave et al. (2013b) with an analysis of *XMM-Newton* data suggests clumpy wind structures of the supergiant's wind.

We have also analyzed the out of eclipse spectra, whenever available in the same observation along with the eclipse. We try to infer the X-ray wind characteristics of these systems, which is the main reprocessing agent in the high mass X-ray binaries.

2. OBSERVATION AND DATA ANALYSIS

XMM-Newton was launched in December 1999. The X-ray observatory consists of 3 sets of co-aligned X-ray telescope each with an effective area of 1500 cm² with the following focal plane instruments: three European Photon Imaging Camera (EPIC) and two Reflection Grating Spectrometers (RGS). Two of the cameras are made of Metal Oxide Semi-conductor (MOS) CCD (Turner et al. 2001) arrays and one uses pn CCDs (Strüder et al. 2001). The pn camera is placed at the focal plane of one telescope and

the two MOS cameras along with the RGS are placed at the focal plane of the other two telescopes. There is one co aligned Optical/UV Monitor (OM) telescope (Mason et al. 2001) which provides simultaneous optical and UV coverage with the X-ray instruments.

According to the observation requirements different read out modes can be selected (Lumb, ScharTEL & Jansen 2012), namely full frame; large window; small window; and Timing mode. The MOS and pn cameras provide imaging over the 30' field of view in the energy range of 0.15–15 keV with a spectral resolution of 20–50 (E/ Δ E) and angular resolution of 6".

The Burst Alert Telescope (BAT) (Barthelmy et al. 2005) onboard the *Swift* mission (Gehrels et al. 2004) observatory is a coded mask aperture instrument with CdZnTe (CZT) detector with a field of view (FOV) of 100°×60°. It operates in the energy range of 15–150 keV with a detection sensitivity of 5.3 mCrab in one day of observation time (Krimm et al. 2013a). We have used long term satellite orbit-wise light curves to identify the eclipse phases of the eclipsing HMXBs.

We used the catalogue of Liu, van Paradijs & van den Heuvel (2000) to select eclipsing HMXBs and then searched for the available EPIC pn observations. We short-listed all EPIC pn observations covering eclipse comparing with the long term *Swift*-BAT orbital profiles (Left figures in Figure 1–11). We found eclipse observations of 9 HMXBs with a total of 13 observations, 11 of which were carried out in the imaging mode, the other two are with Timing mode. The details of the mode of operation are given in Table 2. We used the *XMM-Newton* Science Analysis Software (SAS) version 14.0.0 to reduce the data. We followed Guainazzi et al. 2014¹ and Kirsch et al. (2006) for the data reduction and region selection for the observations with TIMING mode. We followed SAS threads^{2,3,4} for the extraction of the lightcurve and spectra from the cleaned event of the data. We extracted the event files with the SAS tool EVSELECT. We checked for flaring particle background and did not find it in any of the observations. We extracted the events in the energy range of 0.3–12 keV. We first extracted the lightcurve for the whole duration of each observation, then identified the eclipse and out-of-eclipse (whenever available) duration comparing it with the long term average BAT orbital profile and extracted the eclipse and out-of-eclipse events. From these events we extracted source along with background images for each observation. Seeing the image quality we decided the size of the source region to avoid contribution from excess background counts and edge of a CCD. In case of observations with imaging mode we extracted (18–30)" circular source regions. For each observation we extracted circular background region of same size of the source region from a region which is free from any other X-ray sources. In case of Timing mode we extracted box regions with 33≤RAWX≤42 for the source and 3≤RAWX≤5 for the background for one observation (ID 0203500201) of LMCX-4, with 28≤RAWX≤42 for the source and 4≤RAWX≤6 for the background for one ob-

servation (ID 0083280401) of 4U 1700–377. The Timing mode observation of 4U1700–377 was carried out with FastBurst submode. For this observation we extracted the regions with RAWY≤140 (Kirsch et al. 2006).

Many times the data is affected by pile-up. Pile-up causes energy of two photons detected within one CCD exposure to be added, thus it reduces the number of soft X-ray photons and increases the number of hard X-ray photons, leading to an artificial hardening of the spectrum. Hence correction for the pile-up is essential. For EPIC pn observations with FullWindow, LargeWindow, SmallWindow modes the maximum count-rate above which pile-up becomes important are 2(4), 3(6), 25(50) for 2.5(5)% flux loss (Jethwa P. 2012) respectively. However, it is recommended to use the SAS task EPATPLOT, to check the effect of pile-up in the data⁵. We did not notice pile-up in the eclipse data, as the count rate was quite low, compared to the out-of-eclipse phases. For some of the observations during out-of-eclipse phases we noticed pile-up (Cen X-3, OB ID: 0111010101; LMC X-4, OB ID: 0142800101; SMC X-1, OB ID: 0011450101), with the application of the task EPATPLOT. The central part is most likely to be affected by pile-up for pointed observations. For the observations affected by pile up, we first removed the part of the point spread function affected by pile-up, by removing pixels of central 5" region and obtained spectra. We then extracted spectra from an annular source region of inner radius 10". We found stable spectral parameters for same best fit model in both the cases, then finally we obtained the spectra with annular source regions of 5" inner radius for the observations in which we noticed pile-up.

2.1. EVENT SELECTION FROM THE LIGHTCURVES

We extracted source and background lightcurves from the source and background region files respectively from the single and double events (with PATTERN≤4) for the full exposure time for each observation with the SAS task EVSELECT. We subtracted the background lightcurve from the source lightcurve to obtain background subtracted source lightcurve using the FTOOL LCMATH. We confirmed the eclipse and the out-of-eclipse phases (whenever available) by plotting the EPIC pn lightcurve along with the average orbital profile of the long term *Swift*-BAT lightcurve (Krimm et al. 2013b) for each observation. In the left panels of Figure 1–11 the top panels show the long term *Swift*-BAT orbital profiles and the bottom panels the EPIC pn lightcurves. We mark the duration of eclipse events within two solid lines and that of the out-of-eclipse persistent phases within two dashed lines.

Then we extracted separately 1) eclipse events 2) out-of-eclipse persistent events from the event files, for the observations which cover both the eclipse and the out-of-eclipse phases. The observations which were taken during eclipse phases only, we extracted eclipse spectra from the full event files of those observations. To generate the eclipse and out-of-eclipse event files we first noticed the start and end time of each phases, then used the SAS task GTIBUILD to generate good time intervals of the two phases. Then using the SAS task EVSELECT we extracted the eclipse and out-of-eclipse events (whenever available) for each observation.

2.2. SPECTRAL ANALYSIS

¹ XMM-Newton Calibration Technical Note (XMM-SOC-CAL-TN-0083, Nov 14, 2014)

² <https://www.cosmos.esa.int/web/xmm-newton/sas-thread-timing>

³ <https://www.cosmos.esa.int/web/xmm-newton/sas-thread-pn-spectrum>

⁴ <https://www.cosmos.esa.int/web/xmm-newton/sas-thread-pn-spectrum-timing>

⁵ <https://www.cosmos.esa.int/web/xmm-newton/sas-thread-epatplot>

Table 2
The *XMM-Newton* EPIC pn log of observations of the HMXBs

Source	Observation ID	Date of observation	Datamode	Submode	Effective Exposure (s)	Average count-rate (c/s) (OOE)
Cen X-3	0111010101	27-01-2001	IMAGING	PrimeSmallWindow	67250	41.37
LMC X-4	0142800101	09-09-2003	IMAGING	PrimeSmallWindow	113171	51.05
LMC X-4	0203500201	16-06-2004	TIMING	FastTiming	41360	43.21
SMC X-1	0011450101	31-05-2001	IMAGING	PrimeFullWindow	56389	54.57
4U 1700–377	0083280401	20-02-2001	TIMING	FastBurst	30448	22.05
4U 1700–377	0600950101	01-09-2009	IMAGING	PrimeFullWindow	49533	-
4U 1538–522	0152780201	14-08-2003	IMAGING	PrimeFullWindow	79035	10.33
IGR J18027–2016	0745060401	11-09-2014	IMAGING	PrimeFullWindow	43041	2.89
IGR J17252–3616	0405640201	29-08-2006	IMAGING	PrimeLargeWindow	20672	-
IGR J17252–3616	0405640601	08-09-2006	IMAGING	PrimeFullWindow	12104	-
IGR J17252–3616	0405641001	27-09-2006	IMAGING	PrimeLargeWindow	10172	-
IGR J16479–4514	0512180101	21-03-2008	IMAGING	PrimeSmallWindow	32752	-
IGR J16418–4532	0679810101	01-09-2012	IMAGING	PrimeLargeWindow	18281	-

OOE: Out-of-eclipse

We extracted the spectra for both the eclipse and the out-of-eclipse phases (when available), from the single and double events (with PATTERN \leq 4) excluding the events which are at the edge of a CCD and at the edge to a bad pixel (with FLAG=0). For the extraction of the spectra we used the SAS task EVSELECT. We generated response and ancillary files using the SAS task RMFGEN and ARFGEN respectively. We then extracted spectra from these eclipse events for each observation and from the events during out of eclipse persistent phases whenever available. We rebinned the spectra with 25 counts per bin with the SAS routine SPECGROUP and therefore used χ^2 statistics. Observations with IDs 0405640201, 0405640601, 0405641001 of IGR J17252–3616 and 0679810101 of IGR J16418–4532 and 0600950101 of 4U 1700–377 were taken only during eclipse, observation 0512180101 of IGR J16479–4514 covers a small part of the ingress along with total eclipse phase. So for these 6 observations no out-of-eclipse spectra are available. We fitted the X-ray spectra using XSPEC v12.8.2.

The out-of-eclipse spectra and the eclipse spectra are shown in the top panels of each figures at right in Figure (1-5) and in Figure (7 and 8) where the middle and the bottom panels show the contribution of each bin towards the χ for the out of eclipse and eclipse spectra respectively. The top right panel of Figure 6 and Figure (12-11) show the eclipse spectra of these 6 observations where the bottom panels show the contribution of χ for each bin for the eclipse spectra only.

2.2.1. ECLIPSE AND OUT-OF-ECLIPSE SPECTRA OF THE HMXBs

The eclipse spectra were primarily fitted with XSPEC model *powerlaw* modified by photoelectric absorption with model *phabs* to account for the Galactic line of sight and local absorption and a high energy cut-off (XSPEC model *highcut*) for some sources. A few of the sources showed excess low energy emission and a blackbody component (XSPEC model *bbodyrad*) was added to the model for these sources. Excess narrow emission profiles were seen in some of the spectra at specific energies. The excess at specific energies were fitted with Gaussian functions (XSPEC model *gauss*). Some sources show a significant soft excess below 1.5 keV while the power-law component is highly absorbed. The soft excess, therefore

cannot originate at the same location as the power-law for these observations. We have fitted the soft excess as a blackbody (XSPEC model *bbodyrad*) with a different absorption column density in those observations (model *phabs*), only for the purpose of characterizing its temperature and flux. If the soft excess originates in a much larger region elsewhere in the binary, its true nature may not be a blackbody and a bremsstrahlung may be a more appropriate description. For the spectra in which soft excess could not be fitted with blackbody, XSPEC model *bremss* have been used. We note that several eclipse spectra showed a very low even a slightly negative photon index in the 1-10 keV band. However, this does not lead to large bolometric luminosity as the accretion powered pulsars have an exponential cut-off, which is usually above 10 keV and outside the EPIC pn energy band. The details of the models can be found online in HEASARC webpage⁶. The best fit parameters for the eclipse and the out-of-eclipse spectra for all eclipsing HMXBs and details of individual sources are discussed below.

Cen X-3:

Ebisawa et al. (1996) carried out spectral analysis of *ASCA* data in pre-eclipse, ingress, eclipse and egress phases in two energy bands (0.7-4 and 5-10 keV). In the high energy band they obtained best fits with a cut-off powerlaw modified with photoelectric absorption along the line of sight, an Fe edge (\sim 7.1-7.2 keV) and four Gaussian functions for Fe K_{α} (\sim 6.4 keV, \sim 6.7 keV, and \sim 6.97 keV) and Fe K_{β} (fixed with 7.06 keV) emission lines. In low energy band, they fitted the above spectra with absorbed powerlaw with 4-6 emission lines. The broad band (0.5-70 keV) eclipse and out-of-eclipse spectra of Cen X-3 with *Suzaku* (Naik, Paul & Ali 2011) were well fitted with partial covering powerlaw model with high-energy cutoff and Gaussian functions for the three Fe emission lines (6.4 keV, 6.7 keV, and 6.97 keV). Naik & Paul (2012) have obtained best fit with *XMM-Newton* eclipse and out-of-eclipse spectra in the energy range of (4-10 keV) with powerlaw and three Gaussian functions for the above three Fe emission lines. Powerlaw photon index were found to be the lowest in the eclipse phase

⁶ <https://heasarc.gsfc.nasa.gov/xanadu/xspec/manual/Models.html>

which then increases with the increase of flux.

The EPIC pn observation of Cen X-3 (OB ID: 0111010101) covers a large fraction of the total eclipse, eclipse egress and a small part of the out-of-eclipse persistent phase. The eclipse spectrum of this observation was best fitted with a powerlaw, a blackbody emission (bbodyrad), and 8 Gaussian functions for emission lines at 0.98, 1.43, 1.98, 2.62, 3.34, 6.41, 6.66, 6.94 keV modified by photoelectric absorption. The out-of-eclipse spectrum has been fitted with the same model used for the best fit of the eclipse spectrum but with different model parameters. The details are given in Table 3, 4 and 5. In the out-of-eclipse phase the powerlaw photon index is slightly smaller, total flux in the energy range of (0.3-10) keV is larger by a factor of ~ 10 compared to the eclipse phase. We have detected 3 Fe emission lines (fluorescent Fe K_α , Fe XXV and Fe XXVI) in both the eclipse and the out-of-eclipse phases. The flux for the three lines are 0.88, 2.12, 1.65 respectively in the eclipse phase and 15.01, 11.64, 9.58 respectively in the out-of-eclipse phase in units of 10^{-4} photons cm^{-2} sec^{-1} . The corresponding equivalent widths are $\sim 104_{-11}^{+9}$ eV, $\sim 246_{-12}^{+10}$ eV, $\sim 209_{-11}^{+11}$ eV in the eclipse phase, and $\sim 189_{-8}^{+12}$ eV, $\sim 131_{-7}^{+5}$ eV, 139_{-7}^{+7} eV in the out-of-eclipse phase respectively. The Fe K_α emission line flux increases more than 17 times and the corresponding equivalent width increases by a factor of ~ 2 in the out-of-eclipse phase than the eclipse phase. An increase of the equivalent width in the out-of-eclipse phase from the eclipse phase is not expected when the emitting material is distributed in an extended region. The fluxes of the Fe XXV and Fe XXVI emission lines increase by a factor of more than 5 but their equivalent widths fall by a factor of ~ 2 in the out-of-eclipse phase compared to their values in the eclipse phase. An increase of equivalent width of fluorescent Fe K_α emission lines has been observed in the out-of-eclipse phase compared to the eclipse phase earlier from the same *XMM-Newton* observation (Naik & Paul 2012) and from an *ASCA* observation of Cen X-3 (Ebisawa et al. 1996).

LMC X-4:

Naik & Paul (2004b) reported three different fits of the *BeppoSAX* spectra in the low state of LMC X-4, amongst which the fit with powerlaw, a bremsstrahlung component (kT ~ 0.4 keV) and a Gaussian function for 6.4 keV Fe emission line, together modified with line of sight photoelectric absorption is reported to be the best. The best fit for the high state of *BeppoSAX* spectra were obtained with two absorbed powerlaws (hard with $\Gamma \sim 0.65$, soft with $\Gamma \sim 3$), a blackbody component (kT ~ 0.15 keV) and a Gaussian function for 6.4 keV Fe emission line. Neilsen et al. (2009) have obtained the *XMM-Newton*-RGS and *Chandra*-High-Energy Transmission Grating Spectrometer (HETGS) spectra in hard and low state of LMC X-4 respectively. They obtained a best fit of the RGS spectra with powerlaw, bremsstrahlung (kT ~ 0.455 keV), blackbody (kT ~ 0.043 keV) components and Gaussian functions for many emission lines of Nitrogen and Oxygen, all modified with line of sight photoelectric absorption. HETGS spectra gave the best fit with a model comprises of powerlaw, bremsstrahlung (kT ~ 0.43 keV) and Gaussian functions corresponding to different species of emission lines of Neon, Nitrogen, Oxygen and three Fe K_α emission lines, modified with photoelectric

absorption

We have analyzed two EPIC pn observations of LMC X-4, where first one was observed on 9th September 2003 and the second one was observed on 16th June 2004. The first EPIC pn observation of LMC X-4 (OB ID: 0142800101) covers three pre-eclipse bursts, out-of-eclipse persistent emission, eclipse ingress, full length of the total eclipse and eclipse egress. The other observation of this source (OB ID: 0203500201) included out-of-eclipse persistent phase, eclipse ingress, full length of the total eclipse including a small burst and eclipse egress phases. In the first EPIC pn observation (OB ID: 0142800101) of LMC X-4 there were three bursts at the beginning of the observation. For the out-of-eclipse spectrum for this observation we excluded the period of the bursts and only used data where the source intensity was steady, as shown by the dashed lines in the left panel of Figure 2. The pulse profile evolution of LMC X-4 during and after the flares has been reported from this observation by Beri & Paul (2017). In the other observation (OB ID: 0203500201) of LMC X-4 a small burst has been found during eclipse, we extracted the eclipse spectrum for this observation excluding the events during the bursts. The eclipse spectrum of the first observation (OB ID: 0142800101) of LMC X-4 is fitted with a powerlaw, a blackbody and a Gaussian function for the Fe K_α emission line modified by line of sight photoelectric absorption. The X-ray spectrum of LMC X-4 shows very low absorption column density (N_H). N_H could not be constrained with the *XMM-Newton* spectrum. The X-ray spectrum of LMC X-4 detected down to 0.1 keV with the LECS instrument of *BeppoSAX* (Naik & Paul 2004b) with very low N_H . We have taken the Galactic column density of 0.06×10^{22} cm^{-2} towards LMC X-4 (HEASARC TOOL⁷) as lower limit of the absorption column density for the X-ray spectrum. The powerlaw photon index has been obtained to be $0.0_{-0.3}^{+0.3}$ for the eclipse spectrum. The best fit value for the energy of the fluorescent Fe K_α emission line is 6.36 keV with a flux of 0.07×10^{-4} photons cm^{-2} sec^{-1} . For the out-of-eclipse spectrum of this observation the best spectral fit is obtained with model consisting of a power-law, a blackbody emission, a bremsstrahlung radiation and two Gaussian functions (one for Fe XXV emission line another for a low energy emission line), modified by photoelectric absorption. N_H is frozen with the same value as for the eclipse spectrum. Beri & Paul (2017) obtained similar parameters with this model, in the best fit of the phase averaged persistent spectrum of the same EPIC pn observation. In the out-of-eclipse phase, the power law photon index increases by ~ 0.7 , the total flux in the energy range of (0.3-10) keV is larger by factor of more than 237 compared to the eclipse phase. Lowly ionized (or neutral) Fe K_α emission line has been detected during eclipse with high equivalent width (597_{-256}^{+171} eV) but it is absent in the out-of-eclipse phase (upper limit of equivalent width ~ 20 eV), while highly ionized 6.60 keV Fe XXV emission line has been detected in the out-of-eclipse phase, with line flux of 4.03×10^{-4} photons cm^{-2} sec^{-1} and equivalent width of $\sim 166_{-11}^{+12}$ eV, but it is absent in the eclipse phase. We have obtained a low energy emission line with energy $0.96_{-0.01}^{+0.01}$ keV. Neilsen et al. (2009) have detected 13.560 Å (0.91 keV) Ne IX He $_\alpha$ and 12.158 Å (1.02 keV) Ne X Ly $_\alpha$ emission line near 1 keV with the *Chandra* HETGS. The 0.96

⁷ <https://heasarc.gsfc.nasa.gov/cgi-bin/Tools/w3nh/w3nh.pl>

keV line detected by EPIC pn could be a mix of the two lines at 0.91 keV and 1.02 keV of Ne seen earlier with the HETGS instrument.

The second observation of LMC X-4 (OB ID: 0203500201) was carried out in Timing mode. The best fit model for the eclipse spectrum of this observation is obtained with a powerlaw and a blackbody emission modified by photoelectric absorption. The line of sight Hydrogen column density is fixed with $0.06 \times 10^{22} \text{ cm}^{-2}$ for the eclipse spectrum similar to the eclipse and the out-of-eclipse spectrum of the previous observation of this source. The out-of-eclipse spectrum of this observation was best fitted with a powerlaw, a bremsstrahlung radiation and 3 Gaussian functions of emission energies 0.98, 6.38, 6.99 keV, modified by photoelectric absorption with N_{H} frozen with a value of $0.06 \times 10^{22} \text{ cm}^{-2}$. The powerlaw photon index in the out-of-eclipse phase increases by ~ 0.8 , while total flux in the energy range of (0.3-10) keV is larger by a factor of 86 compared to the eclipse phase. We have detected fluorescent Fe K_{α} emission line in the out-of-eclipse phase with a flux of 1.55×10^{-4} photons $\text{cm}^{-2} \text{ sec}^{-1}$ and the equivalent width of $\sim 117_{-2}^{+2}$ eV. Fe XXVI emission line has been detected in the out-of-eclipse phase with a flux of 2.39×10^{-4} photons $\text{cm}^{-2} \text{ sec}^{-1}$ and an equivalent width of $\sim 195_{-3}^{+4}$ eV respectively. In the eclipse spectrum we found some positive residuals in (6-7) keV energy range, but due to poor statistics we could not constrain the energy of the emission lines. However just to compare the line fluxes, we fitted the eclipse spectrum with the two Fe emission lines (fluorescent Fe K_{α} and Fe XXVI), freezing the line energy and width as obtained in the out-of-eclipse spectrum. Including these lines we have obtained very little improvement of χ^2 from a value of 103.01 for 94 degrees of freedom to 99.93 with 92 degrees of freedom. We have found a flux of 2.59×10^{-6} photons $\text{cm}^{-2} \text{ sec}^{-1}$ for fluorescent Fe K_{α} emission line and a flux of 2.80×10^{-6} photons $\text{cm}^{-2} \text{ sec}^{-1}$ for Fe XXVI emission line respectively, which are less significant than 3σ . Like the out-of-eclipse phase of the previous observation, $0.98_{-0.03}^{+0.03}$ keV emission line could be a sum of the two Ne lines as detected by Neilsen et al. (2009) with *Chandra* HETGS.

SMC X-1:

Naik & Paul (2004a) have fitted the pulse phase average spectra with *BeppoSAX* by a hard powerlaw component with high energy cut-off, a blackbody emission for the soft excess and a Gaussian function for 6.4 keV Fe emission line modified by photoelectric absorption. Hu et al. (2013) analyzed both the hard and soft state spectra of SMC X-1 with *RXTE*-PCA. They best describe the continuum of both the spectra with a Comptonized component, a blackbody emission and a Gaussian line of 6.4 keV Fe emission line. They found lower plasma temperature, Fe line width and equivalent width in the low state than in the hard state.

The EPIC pn observation of SMC X-1 (Observation ID: 0011450101) covers a very small portion of the out-of-eclipse persistent phase, eclipse ingress and full length of the total eclipse. The eclipse spectrum of SMC X-1 has been modeled with a powerlaw with high energy cut-off, a blackbody emission and a Gaussian function for Fe K_{α} emission line of 6.38 keV modified by photoelectric absorption. The high energy cut-off was found to have a value of 2.46 keV with a folding energy of 3.6 keV. The

best fit for the out-of-eclipse spectrum is found with the above model except the Fe K_{α} emission line. The high energy cut-off is found to have a value of 2.59 keV with a folding energy of 8.12 keV. The powerlaw photon index has a negative value ($\Gamma = -0.56$) in the eclipse phase and it increases to 0.2 in the out-of-eclipse phase. We also obtain a good fit for the eclipse spectrum with the same model as mentioned above for this phase with the same powerlaw photon index (0.2) as obtained for the best fit of the out-of-eclipse spectrum, but with the parameters for the high energy cut-off and folding energy nearly doubling their values. χ^2 (194.10) for this fit is higher than χ^2 (181.73) of the previous fit. So we report the parameter values in Table 4 and 5 from the previous fit only. The total flux in the energy range of (0.3-10) keV in the out-of-eclipse phase is larger by a factor of ~ 77 compared to its value in the eclipse phase. During the eclipse phase we have detected a fluorescent Fe K_{α} emission line with flux and equivalent width of 0.07×10^{-4} photons $\text{cm}^{-2} \text{ sec}^{-1}$ and 126_{-18}^{+18} eV respectively. We could not detect any Fe K_{α} emission line during the out-of-eclipse phase, but we can not rule out the line as the duration of the out-of-eclipse phase compared to the eclipse phase is very short (lower by a factor of ~ 44) and the continuum flux is higher by a large factor (~ 77 times) in the out-of-eclipse phase from the eclipse phase. We derived an upper limit of equivalent width of ~ 90 eV for an emission line of 6.4 keV.

4U 1700–377:

van der Meer et al. (2005b) have obtained three different fits for the continuum of eclipse, eclipse egress and low flux spectra of 4U 1700–377 with *XMM-Newton*. The first model comprises of three powerlaw components, one for the direct X-rays from the compact object, another for the scattered X-rays from the surrounding medium and the third one is for the soft excess. While the second model is described with first two powerlaws modified with high energy cut-off and in the third model powerlaw for the soft excess was replaced with a blackbody component. Several Gaussian functions were included for the emission lines in all the spectra. The three fits gave similar reduced χ^2 . Amongst possible Fe emission lines 6.4 keV and 6.53 keV Fe K_{α} and 7.06 keV Fe K_{β} emission line have been found during eclipse, while 6.42 keV, 6.72 keV and 7.11 keV Fe emission lines were observed in the egress and 6.41 keV, 6.72 keV (fixed) and 7.06 keV (fixed) Fe emission lines were detected in the low flux state. 6.53 keV Fe emission line seen during eclipse was suggested to come from higher ionized Fe ions (Fe XVIII-XXIV). The relation between the ionization parameters for different lines and the line intensities indicate photoionized plasma surrounding the central source. The fit of the soft excess could not give satisfactory explanation of its origin. Previously with *GINGA*, the soft excess was fitted with bremsstrahlung component (Haberl & Day 1992; Haberl, Aoki & Mavromatakis 1994), the temperature of which could not be constrained.

We have analyzed two EPIC pn observations of 4U 1700–377 (OB IDs: 0083280401, 0600950101) carried out on 20-21 February 2001 for ~ 30 ks and on 1st September 2009 for ~ 50 ks respectively. The first one covers some part of the eclipse, the eclipse egress and a small portion of the out-of-eclipse persistent phase and the second one covers nearly full length of the eclipse phase. The first observation (OB ID: 0083280401) was carried out in Timing

FastBurst mode. For the eclipse spectrum in this observation, the best fit has been obtained with a powerlaw and a Gaussian function with energy 6.37 keV modified by photoelectric absorption. This observation includes a shorter duration of the eclipse and the spectrum has limited statistics. The best fit for the out-of-eclipse spectrum of this observation is also obtained with the above model. The powerlaw photon index has a negative value (-0.41) during eclipse. In the out-of-eclipse phase it increases by ~ 0.24 and is consistent with a range of (-0.72, 0.35). The total flux in the energy range of (0.3-10) keV is large by ≥ 8 times compared to the eclipse phase. During eclipse 6.37 keV Fe K_{α} emission line flux has been found to be 5.96×10^{-4} photons $\text{cm}^{-2} \text{sec}^{-1}$ with a very high equivalent width of $\sim 1258^{+101}_{-103}$ eV. During out-of-eclipse phase the flux for 6.44 keV Fe K_{α} emission line is found to be 14.88×10^{-4} photons $\text{cm}^{-2} \text{sec}^{-1}$ which is ~ 2.5 times higher than its value during eclipse and the equivalent width decreases by a factor of ~ 6.6 to ~ 191 eV.

The eclipse spectrum from the second pn observation (OB ID: 0600950101) has been fitted with a powerlaw modified with high energy cut-off, blackbody emission and 13 Gaussian functions with energies 0.81, 1.28, 1.75, 1.97, 2.34, 2.57, 2.99, 3.70, 4.12, 6.39, 6.68, 7.05 and 7.49 keV modified by photoelectric absorption. The best fit is obtained with the addition of an edge at 7.06 keV. The powerlaw photon index is found to have a negative value of -1.34. Value of the high energy cut-off is determined to be 5.58 keV with a folding energy of 4.59 keV. The fluorescent Fe K_{α} emission line flux has been found to be 4.89×10^{-4} photons $\text{cm}^{-2} \text{sec}^{-1}$ with very high equivalent width of $\sim 1061^{+13}_{-13}$ eV. The Fe XXV emission line flux has been found to be low, 0.26×10^{-4} photons $\text{cm}^{-2} \text{sec}^{-1}$ with very small equivalent width of $\sim 22^{+4}_{-3}$ eV. 7.05 keV emission line flux and equivalent width have been found to be 0.88×10^{-4} photons $\text{cm}^{-2} \text{sec}^{-1}$ and $\sim 219^{+25}_{-32}$ eV respectively.

In the eclipse spectrum of the second pn observation we have detected many emission lines while in the eclipse spectrum of the first observation we have detected only one emission line. The eclipse duration covered in the first observation was significantly shorter than that in the second observation. We checked for the upper limits of the emission lines which were not detected in the eclipse spectrum of the first observation and we have found low upper limit of equivalent width of those lines. We can say, that because of limited statistics we could not constrain other emission lines in the eclipse phase of the first observation. The emission lines in 4U 1700–377 have been discussed by van der Meer et al. (2005b). In this work we restrict our discussion to the Fe lines that are common in most HMXBs.

4U 1538–522:

Mukherjee et al. (2006) have obtained out-of-eclipse spectral analysis of the source with *RXTE* and *BeppoSAX* at two different orbital phases. They obtained best fit of *RXTE* (3-10 keV) data with powerlaw with high energy cut-off and 6.4 keV Fe K_{α} emission line modified by photoelectric absorption. While with *BeppoSAX* in the energy range of 0.3-10 keV they obtained the best fit with the same model except the high energy cut-off. They have not seen any significant variation of the photon index and Fe line flux over the orbital phase with orbital

phase resolved spectral analysis while they have found large variation of column densities along the orbital phase which increases even more just before and after the eclipse asymmetrically. They suggest nearly constant accretion rate and slightly asymmetric condition of the accretion column due to trailing accreting material from the supergiant. Rodes-Roca et al. (2011) have obtained orbital phase averaged and also the eclipse spectra with the same *XMM-Newton* observation of 4U 1538–522. They reported the best fit of the phase averaged spectra with three absorbed powerlaws (with same photon indices but different normalization and column densities) and 4 Gaussian functions for fluorescent ~ 6.4 keV Fe K_{α} , ~ 2.42 keV, ~ 1.90 keV, ~ 1.34 keV emission lines. They obtained best fit for the eclipse spectra with two absorbed powerlaws and 6 Gaussian functions for ~ 6.4 keV fluorescent Fe K_{α} , ~ 6.63 keV Fe XXV, ~ 2.44 keV, ~ 2.00 keV, ~ 1.85 keV, ~ 1.34 keV emission lines. They have identified the low energy emission lines from different species of Sulphur (S), Silicon (Si) and Mg (Magnesium) ions (Table 3 and 6, Rodes-Roca et al. 2011). A soft excess was observed below 0.5 keV, which could neither be satisfactorily explained by a soft powerlaw nor by blackbody emission.

The EPIC pn observation of 4U 1538–522 (OB ID: 0152780201) covers a small part of the out-of-eclipse persistent phase, eclipse ingress and full length of the total eclipse. The eclipse spectrum of this observation is best fitted with a powerlaw, 7 Gaussian functions with energies 1.26, 1.85, 2.40, 6.02, 6.38, 6.69 and 6.95 keV modified by photoelectric absorption. The out-of-eclipse spectrum of this observation got the best fit with a powerlaw and a Gaussian function for fluorescent Fe K_{α} emission line together modified by photoelectric absorption along with a less absorbed blackbody emission. The line of sight equivalent Hydrogen column density associated with the powerlaw emission is $17.16 \times 10^{22} \text{ cm}^{-2}$, while that for the blackbody emission is found to be $0.54 \times 10^{22} \text{ cm}^{-2}$. This value is less by a factor more than 30 than that for the powerlaw emission. The powerlaw photon index in the out-of-eclipse phase increases by ~ 0.5 and the total flux in the energy range of (0.3-10) keV is enhanced by a factor of ≥ 30 compared to its value in the eclipse phase. Both the eclipse and the out-of-eclipse spectrum show the signatures of Fe K_{α} emission line with fluxes of 0.57×10^{-4} photons $\text{cm}^{-2} \text{sec}^{-1}$ and 2.46×10^{-4} photons $\text{cm}^{-2} \text{sec}^{-1}$ with equivalent width of 792^{+42}_{-42} eV and 79^{+22}_{-18} eV respectively. The flux for the Fe K_{α} emission line increases by a factor of ≥ 4 while the equivalent width decreases by a factor of more than 10 in the out-of-eclipse phase from its value in the eclipse phase. Figure 7 shows that the soft X-ray emission in the eclipse and the out-of-eclipse spectra overlaps, corresponding flux in the energy range of 0.3-2.0 keV is obtained as 1.76×10^{-13} ergs $\text{cm}^{-2} \text{sec}^{-1}$ and 2.08×10^{-13} ergs $\text{cm}^{-2} \text{sec}^{-1}$ respectively. The emission lines in 4U 1538–522 has been reported by Rodes-Roca et al. (2011). In this work we confine our discussion to the Fe lines only.

IGR J18027–2016:

Hill et al. (2005) carried out spectral analysis of IGR J18027–2016 with *INTEGRAL* and *XMM-Newton*. With simultaneous fitting of both the spectra they obtained good fitting with an absorbed broken powerlaw and a broad Gaussian for the soft excess. The break was

found at ~ 11 keV and the powerlaw photon indices have values of ~ 0.8 and ~ 3 . Addition of 6.4 keV and 7.1 keV emission lines slightly improves the fit. With pulse phase resolved spectroscopy they have found similar spectral parameters, with high value of line of sight Hydrogen column densities. These indicate that the absorption is not due to neutron star's accretion column and the pulsar is surrounded by supergiant's dense wind. [Aftab, Islam & Paul \(2016\)](#) obtained orbital phase resolved spectroscopy of 33 *Swift*-XRT observations and found a large variation in the source flux, photon index and equivalent Hydrogen column density. This indicates a strongly variable accretion rate of the pulsar and variable wind structures of the supergiant. The detection of several low intensity states along with high states with *Swift*-XRT suggests clumpy wind structures or hydrodynamic instabilities in the accreted material ([Aftab, Islam & Paul 2016](#)).

The EPIC pn observation of IGR J18027-2016 (OB ID: 0745060401) covers a major part of the total eclipse, eclipse egress and some part of the out-of-eclipse phase. The eclipse spectrum of this observation is best fitted with a powerlaw and two Gaussian functions, one for the fluorescent Fe K_{α} emission line of energy 6.41 keV and another of highly ionized 6.66 keV Fe XXV emission line, modified by photoelectric absorption. The N_{H} could not be constrained for the eclipse spectrum. The flux for the Fe K_{α} emission line is found to be 0.07×10^{-4} photons $\text{cm}^{-2} \text{sec}^{-1}$ with an equivalent width of 445_{-191}^{+254} keV. The best fit for the out-of-eclipse spectrum has been obtained with a powerlaw modified by photoelectric absorption only. The powerlaw photon index in the eclipse phase has been found to be $-0.22_{-0.23}^{+0.24}$, which is consistent with a range of $(-0.02, 0.54)$. In the out-of-eclipse phase it increases by ~ 1 and becomes positive (0.71). The total flux in the out-of-eclipse phase in the energy range of (0.3-10) keV is increased by a factor of ≥ 43 .

IGR J17252-3616:

[Manousakis & Walter \(2011\)](#) have fitted the orbital phase resolved *XMM-Newton* spectra with intrinsically absorbed cut-off powerlaw, a blackbody radiation and a Gaussian function for 6.4 keV emission line. The cut-off energy was found to be 8.2 keV with photon index 0.02. The blackbody temperature was 0.5 keV. They have also found Fe K-edge at 7.2 keV. They obtained high and variable intrinsic absorbing column density ($9-89 \times 10^{22} \text{cm}^{-2}$). Fe emission line equivalent width was found to be highly variable, in the range of 40-1100 eV. [Tawara et al. \(1989\)](#) have found strong and variable absorption of the source fitting *GINGA* data with absorbed powerlaw. They found column density upto $\sim 10^{24} \text{cm}^{-2}$. They suggest dense matter surrounding the pulsar. With *GINGA* data, taken ~ 6 months later, [Takeuchi, Koyama & Warwick \(1990\)](#) found a lower value of the column density ($\sim 10^{23} \text{cm}^{-2}$), fitting the spectrum with a power law modified with high energy cut-off. Pulse phase resolved spectroscopy of the source with *INTEGRAL* obtained by [Zurita Heras et al. \(2006\)](#) shows nearly the same continuum emission. [Thompson et al. \(2007\)](#) have fitted the several orbital phase resolved *RXTE* spectra including eclipse with absorbed powerlaw modified by high energy cut-off and a Gaussian function for 6.4 keV Fe emission line. They obtained cut-off of ~ 16 keV for the best fit. They obtained column densities in the range of

$8-126 \times 10^{22} \text{cm}^{-2}$, photon indices in the range of 0.5-2 and huge variation in the 6.4 keV Fe emission line equivalent width (133-6490 eV).

We have analyzed three EPIC pn observations of IGR J17252-3616, all during eclipse phases observed between 29th august-27th September, 2006 (OB IDs: 0405640201, 0405640601, 0405641001). All three observations were initially fitted with powerlaw modified by photoelectric absorption. For the best fit, the first observation needed two Gaussian functions and a less absorbed blackbody emission. One Gaussian is for Fe K_{α} emission line of 6.4 keV and another with a value of 7.01 keV. The second observation was best fitted with the same model as the first observation, except the Gaussian with a value of 7.01 keV. The third observation obtained the best fit with a Gaussian function for Fe K_{α} emission line of energy 6.4 keV. The soft excess in this observation could not be fitted with blackbody emission. The power-law photon index is found to have values of $0.24_{-0.75}^{+0.83}$, $0.81_{-1.17}^{+4.92}$ and $-0.52_{-2.47}^{+4.35}$ respectively in the three observations, while the Fe K_{α} emission line flux is 0.13, 0.18, and 0.04 respectively in units of 10^{-4} photons $\text{cm}^{-2} \text{sec}^{-1}$. The equivalent width is found to be significantly different for the three observations with values of 2695_{-622}^{+415} eV, 1831_{-305}^{+407} eV and 921_{-460}^{+691} eV respectively. The flux and equivalent width associated with 7.01 keV emission line is 0.05×10^{-4} photons $\text{cm}^{-2} \text{sec}^{-1}$ and 1227_{-245}^{+982} eV respectively in the first observation. This is significant $\gtrsim 3 \sigma$. We could not detect this line in the other two observations, as the data is not that good. The line of sight equivalent Hydrogen column density for the power law component for the three observations are 9.34, 18.17 and 13.48 respectively while that for the blackbody component are 0.90 and 2.67 for the first two observations respectively (all values in units of 10^{22}cm^{-2}) which are lower compared to the same for the powerlaw component by a factor of >10 and ~ 7 respectively.

IGR J16479-4514:

[Romano et al. \(2009\)](#) have fitted the out of outburst *Swift*-XRT data with an absorbed powerlaw plus blackbody emission. They suggest a small region on the neutron star surface, perhaps polar cap as the origin of the blackbody emission. [Sidoli et al. \(2013\)](#) have observed the source with *Suzaku* in eclipse and out-of-eclipse phase. They fitted all the spectra with absorbed powerlaw and 6.4 keV Fe emission line. They found hard powerlaw when the source is brighter like other SFXTs and HMXB pulsars. The line of sight column density did not show much variation outside eclipse. The Fe line flux was observed to vary through out the orbit with a correlation with the unabsorbed source flux above 7 keV. Fe line equivalent width was found to increase during eclipse as expected.

The EPIC pn observation of IGR J16479-4514 (OB ID: 0512180101) covers the eclipse ingress and a major part of the total eclipse. We extracted only eclipse spectrum from the total eclipse event for this observation. The eclipse spectrum of this observation is best fitted with a powerlaw, two Gaussian functions with energies 6.41 keV and 6.88 keV modified by photoelectric absorption and a less absorbed blackbody emission associated with the line of sight equivalent Hydrogen column density of

$0.58 \times 10^{22} \text{ cm}^{-2}$ which is a factor of ~ 8 lower than that associated with the powerlaw. The powerlaw photon index is obtained to be $1.28^{+0.37}_{-0.34}$. The Fe K_{α} emission line flux is low with a value of $0.09 \times 10^{-4} \text{ photons cm}^{-2} \text{ sec}^{-1}$ and equivalent width of $803^{+89}_{-89} \text{ eV}$. The energy value for the 6.88 keV emission line is not well constrained like Fe XXVI emission line for other observations (Please see Table 5), the flux for this emission line is $0.05 \times 10^{-4} \text{ photons cm}^{-2} \text{ sec}^{-1}$ with an equivalent width of $576^{+345}_{-230} \text{ eV}$.

IGR J16418–4532:

Romano et al. (2012) obtained the best fit of *Swift*-XRT out-of-eclipse spectra with single absorbed powerlaw. They obtained high intrinsic absorption (upto $\sim 7 \times 10^{22} \text{ cm}^{-2}$). The spectral parameters did not show much variation though the flux variation was quite large. Average spectra based on 2004 and 2011 *XMM-Newton* data were well fitted with an absorbed powerlaw model (Sidoli et al. 2012b). The 2004 data showed marginal evidence of a soft excess below 2 keV. They did not find clear evidence of any Fe emission line. The eclipse spectrum with *INTEGRAL* was fitted with a simple power law with photon index of 2.2 (Drave et al. 2013b). The best fit of the mid-eclipse spectrum with *XMM-Newton* was obtained with an absorbed powerlaw and two Gaussian functions for 6.4 and 6.65 keV Fe emission lines. The post eclipse spectra did not show any evidence of an Fe emission line (Drave et al. 2013b).

The EPIC pn observation of IGR J16418–4532 (OB ID: 0679810101) covers only a major part of the total eclipse. So for this observation we extracted the eclipse spectrum only, which has been fitted with a powerlaw and two Gaussian functions, one for fluorescent Fe K_{α} emission line of 6.43 keV and another for highly ionized Fe XXVI emission line of 6.94 keV, modified by photoelectric absorption. The powerlaw photon index has been found to be $0.40^{+0.83}_{-0.45}$. The Fe K_{α} emission line flux is $0.06 \times 10^{-4} \text{ photons cm}^{-2} \text{ sec}^{-1}$ with a high equivalent width of $1358^{+453}_{-453} \text{ eV}$. The Fe XXVI emission line flux has been found to be $0.05 \times 10^{-4} \text{ photons cm}^{-2} \text{ sec}^{-1}$ with equivalent width of $1911^{+1146}_{-764} \text{ eV}$.

Emission lines other than Fe K_{α} :

We have observed emission lines other than Fe K_{α} in Cen X-3, LMC X-4, 4U 1700–377, 4U 1538–522 and IGR J17252–3616. The line parameters and their previous detections have been given in Table 7. Some of the emission lines were not observed earlier. However, in this work we focus our discussion on Fe emission lines only, so details about other emission lines are not discussed here.

3. DISCUSSION

During the X-ray eclipses, direct emission from the compact object is blocked by the companion and the observed X-rays during eclipses are the reprocessed emission of the primary X-rays from the surrounding medium. For HMXBs, the main reprocessing agent is the stellar wind of the companion and any structures in the wind, if present. The best fit models for all the sources have been given in Table 3. Among the multiple spectral components, the continuum is expected to be strongly suppressed during

the eclipses and the emission lines which are often produced in a larger region in the stellar wind are expected to be suppressed to a lesser extent. The eclipse spectrum is therefore expected to show larger equivalent width and better detectability of the emission lines compared to the out-of-eclipse spectrum. However depending upon the distribution of the material around the compact object and the wind density, this effect can be different in different sources. To investigate the phenomena of X-ray reprocessing in the stellar wind in a large number of HMXBs, and to find if there are significant system to system differences, we have analyzed 13 eclipse observations of 9 HMXBs with the out-of-eclipse observations, whenever available along with the eclipse phases in the same observation. We then compare the eclipse spectra of these sources, and also compare the eclipse and out-of-eclipse spectra whenever available. We have found some similarities and significant differences in the reprocessing properties of the HMXB systems we have analyzed. All these HMXBs have supergiant companions with stellar mass in the range of $\sim 16M_{\odot}$ to $52M_{\odot}$, radius in the range of $8R_{\odot}$ to $26R_{\odot}$ and orbital period of binaries in the range of 1.41 days to 9.74 days. Accretion in three of these systems, LMC X-4, Cen X-3, and SMC X-1 are at least in parts due to Roche Lobe overflow (Savonije 1978; van der Meer et al. 2007).

A summary of the comparison of various aspects of the X-ray reprocessing in these HMXBs is as follows: Equivalent width of the lowly ionized (or neutral) Fe K_{α} emission line during eclipse is found to have a wide range, from $\sim 126^{+18}_{-18} \text{ eV}$ (in SMC X-1, OB ID: 0011450101) to $2695^{+415}_{-622} \text{ eV}$ (in IGR J17252–3616, OB ID: 0405640201) i.e. a factor of >20 larger in the later source. Ratio of the equivalent width of these Fe K_{α} emission line during the eclipse and the out-of-eclipse phases also have a large range, from ~ 0.55 (in Cen X-3) to ~ 10 (in 4U 1538–522). We have compared the best fit models in the energy range of 0.3–10 keV and 3–10 keV. We have found consistent value of the equivalent widths of the Fe lines in eclipse and out-of-eclipse phases. So the error quoted for the equivalent widths are statistical errors only, these do not depend on the choice of the continuum. Flux ratio of the eclipse to out-of-eclipse spectra shows a wide range, from ~ 8 (in 4U 1700–377, OB ID: 0083280401) to ~ 237 (in LMC X-4, OB ID: 0142800101), which differs by a factor of ~ 30 . Even in the same source LMC X-4, the ratio of flux in the out-of-eclipse and the eclipse phase varies as much as by a factor of ~ 3 (from ~ 237 to ~ 86) in different observations. Here we discuss the results of some individual sources.

3.1. Cen X-3:

In Cen X-3 (OB ID: 0111010101), three Fe emission lines i.e. 6.41 keV (fluorescent Fe K_{α}) and 6.66 keV (Fe XXV) and 6.94 keV (Fe XXVI) emission lines have been detected. Equivalent width of Fe XXV and Fe XXVI emission lines have been observed to be higher in the eclipse phase compared to the out-of-eclipse as expected. The equivalent width of the Fe emission lines in this source during eclipse is smaller than for other SgHMXBs with similar line of sight equivalent Hydrogen column density (N_H). Ebisawa et al. (1996) and Naik & Paul (2012) have also found lower equivalent width of Fe emission lines in eclipse compared to out-of-eclipse with *ASCA* and *XMM-Newton* respectively. The wind in Cen X-3 is smooth (Wojdowski, Liedahl & Sako 2001). A low density wind in the surrounding region of the compact object can produce low equivalent width, but why the O type supergiant companion in Cen X-3 has

Table 3

The exposure times for the eclipse and the out-of-eclipse spectra of the HMXBs and the best fit spectral models

Source	Observation ID	Phase	exposure (s)	Best fit model
Cen X-3	0111010101	E	7152	phabs ₁ × (bbodyrad ₂ + gaussian ₃ + gaussian ₄ + gaussian ₅ + gaussian ₆ + gaussian ₇ + gaussian ₈ + gaussian ₉ + gaussian ₁₀ + powerlaw ₁₁)
Cen X-3	0111010101	OOE	8937	phabs ₁ × (gaussian ₂ + gaussian ₃ + bbodyrad ₄ + gaussian ₅ + gaussian ₆ + gaussian ₇ + gaussian ₈ + gaussian ₉ + gaussian ₁₀ + powerlaw ₁₁)
LMC X-4	0142800101	E	8972	phabs ₁ × (powerlaw ₂ + bbodyrad ₃ + gaussian ₄)
LMC X-4	0142800101	OOE	38170	phabs ₁ × (powerlaw ₂ + brems ₃ + bbodyrad ₄ + gaussian ₅ + gaussian ₆)
LMC X-4	0203500201	E	11630	phabs ₁ × (bbodyrad ₂ + powerlaw ₃)
LMC X-4	0203500201	OOE	6336	phabs ₁ × (brems ₂ + gaussian ₃ + gaussian ₄ + gaussian ₅ + powerlaw ₆)
SMC X-1	0011450101	E	30790	phabs ₁ × (highcut ₂ × powerlaw ₃ + bbodyrad ₄ + gaussian ₅)
SMC X-1	0011450101	OOE	808	phabs ₁ × (highcut ₂ × powerlaw ₃ + bbodyrad ₄)
4U 1700–377	0083280401	E	622	phabs ₁ × (powerlaw ₂ + gaussian ₃)
4U 1700–377	0083280401	OOE	34	phabs ₁ × (powerlaw ₂ + gaussian ₃)
4U 1700–377	0600950101	E	42790	edge ₁ × phabs ₂ × (bbodyrad ₃ + gaussian ₄ + gaussian ₅ + gaussian ₆ + gaussian ₇ + gaussian ₈ + gaussian ₉ + gaussian ₁₀ + gaussian ₁₁ + gaussian ₁₂ + gaussian ₁₃ + gaussian ₁₄ + gaussian ₁₅ + gaussian ₁₆ + highcut ₁₇ × powerlaw ₁₈)
4U 1538–522	0152780201	E	44780	phabs ₁ × (powerlaw ₂ + gaussian ₃ + gaussian ₄ + gaussian ₅ + gaussian ₆ + gaussian ₇ + gaussian ₈ + gaussian ₉)
4U 1538–522	0152780201	OOE	3171	phabs ₁ × (gaussian ₂ + powerlaw ₃) + phabs ₄ × bbodyrad ₅
IGR J18027–2016	0745060401	E	22150	phabs ₁ × (powerlaw ₂ + gaussian ₃ + gaussian ₄)
IGR J18027–2016	0745060401	OOE	4347	phabs ₁ × powerlaw ₂
IGR J17252–3616	0405640201	E	19190	phabs ₁ × (powerlaw ₂ + gaussian ₃ + gaussian ₄) + phabs ₅ × bbodyrad ₆
IGR J17252–3616	0405640601	E	10620	phabs ₁ × (powerlaw ₂ + gaussian ₃) + phabs ₄ × bbodyrad ₅
IGR J17252–3616	0405641001	E	9431	phabs ₁ × (powerlaw ₂ + gaussian ₃)
IGR J16479–4514	0512180101	E	18730	phabs ₁ × (gaussian ₂ + gaussian ₃ + powerlaw ₄) + phabs ₅ × bbodyrad ₆
IGR J16418–4532	0679810101	E	16990	phabs ₁ × (powerlaw ₂ + gaussian ₃ + gaussian ₄)

a thinner wind than O and B type supergiants in other HMXB systems, is not understood. The equivalent width of Fe K_α emission line has been found to be lower in the eclipse phase compared to the out-of-eclipse phase as observed by Naik & Paul (2012) and Ebisawa et al. (1996). Fe K_α emission line flux increases by a factor of more than 17 as the source comes out of the eclipse while FeXXV and FeXXVI emission line fluxes increase by a factor of ~5.5 and ~5.8 respectively. Similar result was obtained by Naik & Paul (2012). These observations confirm that most of the fluorescent Fe K_α line emitting region were closer to the source and distributed in a region of size comparable or smaller than the radius of the companion star from the

compact object. Ionization state of the Fe atoms are expected to be high near the compact object because of its intense X-ray emission, but here we see most of the low ionized Fe atoms are closer to the compact object compared to the highly ionized Fe atoms. This is possible if the Fe atoms closer to the source are in very dense optically thick accretion disc or in dense accretion stream. High density of the disc or the stream keeps the Fe atoms lowly ionized in spite of them being near to the source.

3.2. LMC X-4:

Naik & Paul (2004b) have observed the source with *BepoSAX* in low and high states of its superorbital period.

The decrease of the continuum flux was found to be more by a factor of 5 compared to the decrease of 6.4 keV Fe line flux in the low state, which they suggest is caused by a different origin for the continuum and the Fe line emission. The smaller value of Fe line flux and higher value of Fe line equivalent width in the low state indicates that a major part of the line emission is from a region comparable to or smaller than the size of the obscuring material (most probably part of the accretion disk) and also some part of the emission line comes from an extended region. In the low state they have not found any significant increase of the line of sight column density, indicating that the continuum X-ray emission comes from an extended region. The equivalent width of fluorescent Fe K_{α} emission line have been detected during low and high state of the source with 1260 eV and 240 eV respectively. Neilsen et al. (2009) found variable Doppler shift of the Fe lines. They suggest that the origin of the Fe line is the inner accretion disk warp. The evolution of the other emission lines suggests precession of the accretion disk.

During eclipse in the first pn observation of LMC X-4 (OB ID: 0142800101) fluorescent Fe K_{α} emission line has been detected with high equivalent width (597_{-256}^{+171} eV), but this line is absent in the out-of-eclipse phase. The large increase (>237 times) of the total flux in the out-of-eclipse phase perhaps strongly suppressed this emission line which makes it undetectable during the out-of-eclipse phase. Fe XXV emission line has been detected during the out-of-eclipse phase but it is absent in the eclipse phase, which indicates most of the highly ionized wind material which emits Fe XXV photons is distributed in a region less than the distance comparable to the radius of the companion from the compact object. In the second observation of LMC X-4 (OB ID: 0203500201) during eclipse, the detection of fluorescent Fe K_{α} emission line is marginal. However we can not rule out this line as the statistics of the eclipse spectrum of this observation is very poor. During out-of-eclipse phase in the second observation fluorescent Fe K_{α} emission line is comparatively stronger. This indicates most of the lowly ionized Fe atoms were closer to the source during this observation. When the source came out of the eclipse, these Fe atoms showed their presence through the 6.38 keV emission line during the out-of-eclipse phase. This can happen only if these Fe atoms are in the dense accretion disc and/or accretion stream during this observation. Highly ionized 6.99 keV Fe XXVI emission line has also been detected during out-of-eclipse phase of the second observation, but it is insignificant in the eclipse phase, which possibly indicates that the origin of this emission line is very near to the compact object. However due to poor statistics of the eclipse spectrum we can not make any definitive comment about the scenario. Highly ionized Fe XXVI emission line has been detected in LMC X-4 for the first time (OB ID: 0203500201). None of the earlier observations have detected this emission line in this source. We checked for the superorbital phase of the source during the out-of-eclipse phase of this observation and found it in the bright phase, while the other observation (OB ID: 0142800101) of this source shows a low superorbital phase. During eclipse phase in the first observation of LMC X-4, the total flux (0.3-10.0 keV) is lowered by a large factor (>237) from the out-of-eclipse phase, while in the second observation the flux ratio between the out-of-eclipse to eclipse phase is ~ 86 . This signifies a difference in the density and/or spatial distribution of the reprocessing material between these two observations. During eclipse in

the first observation lowly ionized (or neutral) fluorescent 6.36 keV Fe K_{α} emission line has been detected, while in the second observation during eclipse phase the detection of this line is insignificant. In the first observation during the out-of-eclipse phase amongst Fe emission lines only highly ionized 6.60 keV Fe XXV emission line has been detected, in the second observation during out-of-eclipse phase, 6.38 keV Fe K_{α} emission line and highly ionized 6.99 keV XXVI emission line have been detected. These indicate higher ionization of matter near the compact object during the second observation compared to the first observation. Lowly ionized (or neutral) 6.38 keV Fe K_{α} and highly ionized Fe XXVI emission during the out-of-eclipse phase of the second observation indicates a mixture of hot and cold wind near the compact object. Lowly ionized Fe atoms could possibly be distributed in optically thick accretion disk or in the dense accretion stream closer to the source. The high density of the stream makes them lowly ionized in spite of these Fe atoms being near to the source.

3.3. 4U 1700–377:

In all the eclipse, eclipse egress and low flux spectra spectra of 4U 1700–377 van der Meer et al. (2005b) have found a ~ 6.4 keV Fe emission line, they suggest a clumpy wind near the compact object as the origin of this line. The detection of many strong emission lines during eclipse indicates that these lines are originating from an extended region. Also the intensity of some of the emission lines with very high values of their ionization parameters increase towards egress, which indicates that the extension of the ionized plasma around the central source is not very large either.

Two observations of 4U 1700–377 were separated by a span of more than 8 years. In the first observation of 4U 1700–377 (OB ID: 0083280401) lowly ionized fluorescent Fe K_{α} emission line has been detected in both the eclipse and out-of-eclipse phases (6.37 keV and 6.44 keV respectively) which are consistent with energy 6.4 keV. The equivalent width of this Fe emission line during eclipse is found to be much higher as compared to the out-of-eclipse phase, as expected. The emission flux and the equivalent width of this Fe K_{α} emission line detected during eclipse is found to be higher compared to the same in the other observation (OB ID: 0600950101) during eclipse. This signifies greater reprocessing by lowly ionized Fe atoms during this observation compared to the later one. Non-detection of Fe XXV and Fe XXVI emission lines in this observation indicates comparatively colder wind during this observation. Many low energy emission lines have been detected in the eclipse spectrum of the second observation but were not detected in the eclipse phase of the first observation, which could be due to limited statistics.

The second observation of 4U 1700–377 (OB ID: 0600950101) covers only eclipse and in this phase fluorescent Fe K_{α} and highly ionized Fe XXV emission lines have been detected along with other low energy emission lines and an emission line of energy 7.05 keV. This 7.05 keV emission line could be Fe K_{β} line. The ratio of the flux of the Fe K_{β} to Fe K_{α} emission line is $0.18(\eta)$. This indicates ionized medium surrounding the compact object ($\eta \leq 0.125$ for Fe neutral gas Kaastra & Mewe 1993), which is consistent with the detection of the highly ionized Fe K_{α} (Fe XXV) emission line. The equivalent width of fluorescent Fe K_{α} emission line is very high (1061_{-13}^{+13} eV) and that of

the Fe XXV emission line is quite low (22_{-3}^{+4} eV) in this observation. This indicates an ionized medium most of the Fe atoms lower ionized than Fe X are distributed at least at a distance comparable to the radius of the companion star from the compact object during this observation.

3.4. Other sources

Pulse phase resolved spectra of SMC X-1 with *BepoSAX* show a phase shift of the pulsating soft component compared with that of the hard powerlaw component (Naik & Paul 2004a). This suggests different origin of the soft and hard X-rays.

In SMC X-1 a weaker lowly fluorescent 6.38 keV Fe K_{α} emission line has been detected with EPIC pn during eclipse with an equivalent width of 126_{-18}^{+18} eV, which is the lowest equivalent width of the fluorescent Fe K_{α} emission line amongst all the eclipsing sgHMXBs reported in this work. The detection of this line is marginal in the out-of-eclipse phase (with an upper limit of equivalent width of ~ 90 eV). In spite of having good statistics in the eclipse spectra, a weak detection of fluorescent Fe K_{α} emission line could be due to low metallicity of the system

In the eclipse spectrum of 4U 1538–522 with *XMM-Newton*, Rodes-Roca et al. (2011) have found 6.4 keV Fe K_{α} fluorescent and 6.6 keV Fe XXV emission line. They also detected other emission lines with wide range of ionization states. This broad range suggests that the emitting region is either wide or the emitting material have large range of densities. The coexistence of variety of recombination and fluorescent emission lines has also been observed in Vela X-1 during eclipse with *ASCA* and *Chandra* (Sako et al. 1999; Schulz et al. 2002), which suggests an inhomogeneous wind structure with cool, dense clumps scattered in highly ionized plasma.

In 4U 1538–522, the fluorescent Fe K_{α} emission line has been observed in both the eclipse and the out-of-eclipse phase with greater equivalent width during eclipse phase as expected. As pointed out in section 2.2.1, the power-law component in this source is heavily absorbed with a column density of $17.16_{-1.12}^{+1.17} \times 10^{22}$ cm $^{-2}$. A black body component should not be detectable, if it has same column density. We have therefore, fitted with soft excess with a different column density. The line of sight Hydrogen column density for the soft excess is less than that for the powerlaw by a large factor (>30), which indicates that soft X-ray emissions are coming from a different region away from the neutron star. Again nearly equal soft X-ray flux (0.3–2.0 keV) in the eclipse and the out-of-eclipse spectra indicates the origin of the soft X-rays far away (at least further away than the size of the companion) from the compact object and is not blocked during eclipse.

Hill et al. (2005) have obtained a smaller value of the Fe K_{α} emission line equivalent width for IGR J18027–2016 in off and on pulse (40 eV and 25 eV respectively). We detected this Fe emission line with high equivalent width during eclipse (445_{-191}^{+254} eV) in IGR J18027–2016 but has not been detected in the out-of-eclipse phase, which is similar to the observation of SMC X-1 except that the equivalent width in case of SMC X-1 during eclipse phase was found to be low (126_{-18}^{+18} eV).

The observations of IGR J16479–4514, IGR J16418–4532 and the three observations of IGR J17252–3616 covered only the eclipse. In these observations low ionized (or neutral) Fe K_{α} emission lines have been detected with large equivalent widths.

In the first observation (OB ID: 0405640201) of IGR J17252–3616 the equivalent width is found to be largest (2695_{-622}^{+415} eV) amongst all the observations analyzed in this work. Varying equivalent width (921–2695 eV) and flux (0.04–0.18 photons cm $^{-2}$ sec $^{-1}$) of Fe K_{α} emission line in 3 observations of IGR J17252–3616 indicate a change in the distribution and density of lowly ionized Fe atoms surrounding the compact object at least at a distance equal to the radius of the companion over a period of 1 month. Manousakis & Walter (2011) have found spectral variation over the orbital phase of IGR J17252–3616 with *XMM-Newton*. During the eclipse they found a drop of the fluorescent Fe K_{α} emission line equivalent width by a factor >10 , that indicates a cocoon-like wind structure surrounding the compact object. For IGR J16479–4514, Sidoli et al. (2013) also have obtained a high equivalent width (5500_{-3700}^{+4500} eV) of fluorescent Fe K_{α} emission line during eclipse with *Suzaku*, while it is in the range of $40\text{--}280_{-160}^{+160}$ eV outside of the eclipse. Based on *XMM-Newton* data, Sidoli et al. (2012b) obtain a high Fe K_{α} emission line equivalent width of 3100 eV during eclipse.

In the out-of-eclipse phase of the observation of 4U 1538–522, also in the eclipse phase of IGR J16479–4514 and in the first two observations of IGR J17252–3616, the line of sight equivalent Hydrogen column density for the soft X-ray emission are lower by several factor ($\sim 8\text{--}680$) than that for the power law. This signifies a different origin for the hard and soft X-rays in these sources during the observations mentioned above. Detection of a soft excess, even when the power-law component is absorbed by a very large column density of material ($\sim 10^{24}$ cm $^{-2}$) is known in some HMXBs (GX 301-2: Islam & Paul 2014), and it has been attributed to a different origin of the soft component compared to the powerlaw component.

To study the variation of X-ray reprocessing with the orbital parameters of the HMXBs, we show the orbital period of the system, mass, radius and mass loss rate of the companion (through wind), projected semi major axis of the system as functions of out-of-eclipse to eclipse flux ratios (Figure 14). We have not noticed any correlation of these parameters with the flux ratios. In the two observations of LMC X-4, the flux ratios vary by a factor of ~ 3 . In Figure 15 we show a relation between equivalent width (Eqw) of Fe K_{α} emission line and line of sight equivalent Hydrogen column density (N_{H}) obtained during out-of-eclipse phase. We do not see an evident correlation between the two parameters. A direct correlation is expected between Eqw and N_{H} during out-of-eclipse phase, as this line is produced by the fluorescence of X-rays from the compact object where the surrounding medium causes this fluorescence (George & Fabian 1991). Thus, in a denser surrounding medium, more fluorescence is expected to occur. A direct correlation has been observed between the two parameters by Torrejón et al. (2010) and Giménez-García et al. (2015). Out of 7 out-of-eclipse observations we have detected fluorescent Fe K_{α} emission line in 4 observations. In Figure 15 we also show upper limit of the equivalent width of 6.4 keV emission line in other three out-of-eclipse observations. This limited data does not allow a clear conclusion about the relationship between Eqw- N_{H} in SgHMXB systems.

In Figure 16, we have plotted N_{H} for the observations which have both the eclipse and out-of-eclipse data. In this Figure, the X axis indicates the observations and the Y

axis in the top panel shows N_{H} during eclipse (pink boxes) and out-of-eclipse (blue triangles) phases. Y axis in the bottom panel gives the value of 0.3-10 keV out-of-eclipse to eclipse flux ratios. For 3 observations (4U 1700–377 OB ID: 0083280401, 4U 1538–522, IGR J18027–2016) N_{H} is larger during eclipse than out-of-eclipse phase. For the other 4 observations, N_{H} is comparable in both the phases. In Figure 17, we have plotted the out-of-eclipse to eclipse flux ratios with the ratio of line of sight equivalent Hydrogen column densities (N_{H}) during out-of-eclipse and eclipse of the HMXBs, for which both the out-of-eclipse and eclipse data were available. We excluded LMC X-4 from this plot, as the N_{H} could not be constrained for this source. The sources that show large flux ratio between out-of-eclipse and eclipse spectra (SMC X-1, IGR J18027–2016, and 4U 1538–522) probably have less dense wind environment compared to the two source Cen X-3 and 4U 1700–47, as the large out-of-eclipse to eclipse flux ratio indicates lesser reprocessing. Within each type, the sources with low ratio of the column density in the out-of-eclipse and eclipse spectra (SMC X-1 and Cen X-3) probably have more isotropic wind pattern compared to the sources for which the column density is much larger in the out-of-eclipse spectra (4U 1700–37, IGR J18027–2016, and 4U 1538–522). In the later sources, the supergiant companion might have stronger wind outflow in the equatorial (or near equatorial) plane (as shown in Figure 18), the companion could also have a trailing wind as described by Blondin (1994) as shadow wind. These features may explain the differences in column density in the eclipse and out-of-eclipse phases.

Comparison of the fluxes in (0.3-2.0) keV energy range in eclipse and out-of eclipse phases indicate source of the soft excess is near the compact object in our sample of HMXBs except in 4U 1538–522. In 4U 1538–522 the soft excess in both the phases are comparable, which indicates that the soft excess must be originating far away from the system. Spectrum also softens during eclipse, perhaps the soft excess is due to dust scattering in the interstellar medium (ISM) along the line of sight. Robba et al. (2001) has also observed softening of the spectrum during total eclipse compared to the out-of-eclipse phase in 4U 1538–522, they suggest dust-scattering of the direct photon as the origin of the soft excess in the source. Audley et al. (2006) have also found evidence of dust hallow surrounding the eclipsing HMXB OAO 1657–415.

3.5. Comparison of SFXTs and SgHMXBs:

SFXTs have a much lower average X-ray luminosity compared to the SgHMXBs and only become bright during short flares. The compact objects in SFXTs are most probably neutron stars (in’t Zand 2005). The SFXTs show lower equivalent width of Fe K_{α} emission line compared to SgHMXBs outside eclipse (Pradhan, Bozzo & Paul 2018) with *Suzaku* and *XMM-Newton* data. Their findings in a large sample of both the systems suggest that the compact object in the SFXT systems are surrounded by winds less dense than that in SgHMXBs. The compact object in SFXTs is inhibited from accretion from its companion most of the time (Negueruela et al. 2006; Sguera et al. 2005), the low intensity X-ray emission is insufficient to reduce the speed of the supergiant’s radiatively driven wind effectively, hence most of the wind pass by the compact object and lost from the SFXT systems and the compact objects in SFXTs are surrounded by less dense winds. Maccarone, Girard & Casetti-Dinescu (2014) suggests that

some SFXTs might have eccentric orbit, so the compact object spends most of the time away from its supergiant companion and hence surrounded by less dense matter. But as a counterexample, indications of a circular orbit has been found in SFXT IGR J16479–4514 which has an orbital period of ~ 3 days (Jain, Paul & Dutta 2009a; Sidoli et al. 2013). Considering a spherical wind outflow from the supergiant star and from the scattered and direct emission respectively during eclipse and out of eclipse phases an expected luminosity of these sources can be estimated, but this is two orders higher than the observed luminosity (Martínez-Núñez et al. 2017; Sidoli et al. 2013). The usual low luminosity in the SFXT systems can be explained if the neutron star remains in supersonic propeller regime most of the time. This can lower the luminosity by a factor of 100–1000 compared to the case of direct accretion for neutron stars with spin period in the range of 10–100 s and magnetic field with $\mu_{30} = 0.1$ –1 (Martínez-Núñez et al. 2017). If the interaction of the supergiant’s wind with the compact object in these systems is very different than that in SgHMXBs, that also could make the compact object’s environment less dense, which produces low equivalent widths of Fe emission line (Pradhan, Bozzo & Paul 2018).

However the two SFXTs (IGR J16479–4514, IGR J16418–4532) in our sample have Fe line equivalent widths large and comparable to the SgHMXBs during eclipses. IGR J16479–4514 and IGR J16418–4532 have equivalent widths of 803^{+89}_{-89} eV and 1358^{+453}_{-453} eV respectively for the fluorescent Fe K_{α} emission line during eclipses, while the equivalent width of this line for the SgHMXBs is in the range of (126–2695 eV). The equivalent width of the Fe XXVI emission line are 576^{+345}_{-230} eV and 1911^{+1146}_{-764} eV, respectively in the above two SFXTs respectively. The line of sight Hydrogen column density (N_{H}) in these SFXTs are like other SgHMXBs in our sample. During eclipse, both the continuum and the Fe line are reprocessed emission from the same wind material, so a comparable equivalent width of the Fe line in SgHMXBs and SFXTs during eclipse only indicate similar Fe abundance in the two kinds of systems. A lower Fe abundance can possibly explain a lower line equivalent width in SFXTs outside the eclipse (as found by Pradhan, Bozzo & Paul 2018), but such a possibility is ruled out with the current result. We need large samples with multiple observations, during eclipses to interpret the relation between the fluorescent Fe K_{α} emission line equivalent width with luminosity and N_{H} , also to investigate the interaction of the compact object with the supergiant’s wind and hence wind distributions surrounding the compact objects in SFXTs.

4. CONCLUSION

We have found ample diversity in the X-ray reprocessing characteristics in high mass X-ray binaries. The out-of-eclipse to eclipse flux ratio has been found to be in the range of $\sim (8$ –237), which implies significantly dynamic wind structure surrounding the compact object in HMXBs. Even in the same source at different epochs the variation is quite large (86–237 in LMC X-4).

The equivalent widths of Fe emission lines found in SFXTs are large during eclipse, similar to that in SgHMXBs. The equivalent width of the fluorescent Fe K_{α} emission line found in the SFXTs IGR J16479–4514 and IGR J16418–4532 are 803^{+89}_{-89} eV and 1358^{+453}_{-453} eV, respectively. Whereas the equivalent width of the Fe XXVI emis-

sion line have been found to be 576^{+345}_{-230} eV and 1911^{+1146}_{-764} eV respectively in these two SFXTs. Which implies a similar Fe rich medium in SFXTs like in SgHMXBs.

Cen X-3 is one exception for which the equivalent width of the Fe K_{α} emission line is lower during eclipse compared to the out-of-eclipse phase, this indicates an Fe rich, dense accretion disk or accretion stream near the compact object.

In 4U 1538–522 the soft X-ray emission flux is nearly same in out-of-eclipse and eclipse phase, i.e. the soft X-ray emission is not blocked during eclipse of the compact object by the supergiant companion, which clearly indicates a different origin for the hard and soft X-rays. Perhaps dust scattering of the direct photons in ISM, far away from the source are the origin of this soft excess.

Some systems show comparable wind density near and far away from the compact object (Cen X-3, LMC X-4, SMC X-1). There are some indications of equatorial or near equatorial dense wind outflows from the supergiant in three different observations (IGR J18027–2016, 4U 1538–522 and first observation of 4U 1700–377).

Acknowledgements:

This work has made use of archival data obtained from *XMM-Newton* Science Archive (XSA) provided by the European Space Agency (ESA). We have also used the public light curves from the *Swift*-BAT site.

Table 4

Line of sight Hydrogen column density (N_{H}), photon index (Γ) and blackbody temperature (T_{BB}), χ^2/DOF and total flux in the energy range of (0.3-10.0) keV of 9 eclipsing HMXB systems during eclipse (E) and out-of-eclipse (OOE) phases

Source	Observation ID	Phase	N_{H} (10^{22} cm^{-2})	Photon Index (Γ)	T_{BB} (keV)	χ^2 (DOF)	Total Flux (10^{-11} ergs cm^{-2} sec^{-1})
Cen X-3	0111010101	E	$1.50^{+0.10}_{-0.11}$	$0.71^{+0.02}_{-0.06}$	$0.14^{+0.01}_{-0.01}$	197.73 (127)	4.47
Cen X-3	0111010101	OOE	$2.07^{+0.18}_{-0.16}$	$0.51^{+0.05}_{-0.02}$	$0.08^{+0.01}_{-0.01}$	207.39 (137)	43.74
LMC X-4	0142800101	E	0.06 (frozen)	$0.0^{+0.3}_{-0.3}$	$0.22^{+0.03}_{-0.03}$	38.83 (37)	0.11
LMC X-4	0142800101	OOE	0.06 (frozen)	$0.74^{+0.01}_{-0.01}$	$0.044^{+0.005}_{-0.005}$	1129.22 (718)	26.09
LMC X-4	0203500201	E	0.06 (frozen)	$0.08^{+0.20}_{-0.21}$	$0.18^{+0.02}_{-0.01}$	103.01 (94)	0.18
LMC X-4	0203500201	OOE	0.06 (frozen)	$0.88^{+0.04}_{-0.04}$	-	151.81 (145)	15.48
SMC X-1	0011450101	E	$0.03^{+0.02}_{-0.02}$	$-0.56^{+0.23}_{-0.25}$	$0.23^{+0.02}_{-0.01}$	181.73 (147)	0.52
SMC X-1	0011450101	OOE	$0.06^{+0.03}_{-0.03}$	$0.20^{+0.17}_{-0.17}$	$0.21^{+0.02}_{-0.02}$	198.21 (156)	39.84
4U 1700–377	0083280401	E	$0.62^{+1.10}_{-0.62}$	$-0.41^{+0.26}_{-0.24}$	-	88.60 (71)	4.28
4U 1700–377	0083280401	OOE	$23.17^{+19.36}_{-6.36}$	$-0.17^{+0.52}_{-0.55}$	-	23.96 (18)	34.28
4U 1700–377	0600950101	E	$1.01^{+0.32}_{-0.43}$	$-1.34^{+0.14}_{-0.14}$	$0.08^{+0.04}_{-0.06}$	195.06 (133)	3.19
4U 1538–522	0152780201	E	$0.36^{+0.08}_{-0.05}$	$0.22^{+0.06}_{-0.06}$	-	178.19 (130)	0.46
4U 1538–522	0152780201	OOE	$17.16^{+1.17}_{-1.12}$	$0.71^{+0.08}_{-0.08}$	$1.53^{+0.88}_{-0.42}$	125.90 (126)	13.93
IGR J18027–2016	0745060401	E	$0.36^{+0.53}_{-0.36}$	$-0.22^{+0.24}_{-0.23}$	-	49.28 (41)	0.08
IGR J18027–2016	0745060401	OOE	$5.90^{+0.40}_{-0.37}$	$0.71^{+0.08}_{-0.08}$	-	110.04 (110)	3.47
IGR J17252–3616	0405640201	E	$9.34^{+137.59}_{-6.46}$	$0.24^{+0.83}_{-0.75}$	$0.19^{+4.92}_{-0.10}$	6.23 (7)	0.04
IGR J17252–3616	0405640601	E	$18.17^{+24.96}_{-12.15}$	$0.81^{+4.92}_{-1.17}$	$1.07^{+0.01}_{-0.001}$	7.66 (8)	0.05
IGR J17252–3616	0405641001	E	$13.48^{+43.32}_{-13.48}$	$-0.52^{+4.35}_{-2.47}$	-	3.50 (6)	0.03
IGR J16479–4514	0512180101	E	0.58 (frozen)	$1.28^{+0.37}_{-0.34}$	$0.07^{+0.39}_{-0.09}$	44.67 (36)	0.08
IGR J16418–4532	0679810101	E	$0.84^{+1.43}_{-0.84}$	$0.40^{+0.83}_{-0.45}$	-	2.13 (5)	0.03

Table 5
 Fe K_{α} (fluorescent), Fe XXV and Fe XXVI emission line energy, flux and equivalent width for 9 HMXBs during eclipse (E) and out-of-eclipse (OOE) phases. Line fluxes are given in units of 10^{-4} photons $\text{cm}^{-2} \text{sec}^{-1}$.

Source	Observation ID	State	Fe K_{α} line energy (keV)	Fe K_{α} line flux	Fe K_{α} line eqv. width (eV)	Fe XXV line energy (keV)	Fe XXV line flux	Fe XXV line eqv. width (eV)	Fe XXVI line energy (keV)	Fe XXVI line flux	Fe XXVI line eqv. width (eV)
Cen X-3	0111010101	E	$6.41^{+0.05}_{-0.03}$	$0.88^{+0.08}_{-0.09}$	104^{+9}_{-11}	$6.66^{+0.01}_{-0.01}$	$2.12^{+0.09}_{-0.1}$	246^{+10}_{-12}	$6.94^{+0.01}_{-0.01}$	$1.65^{+0.09}_{-0.09}$	209^{+11}_{-11}
Cen X-3	0111010101	OOE	$6.41^{+0.01}_{-0.01}$	$15.01^{+0.93}_{-0.66}$	189^{+12}_{-8}	$6.68^{+0.01}_{-0.01}$	$11.64^{+0.45}_{-0.58}$	131^{+5}_{-7}	$6.98^{+0.01}_{-0.01}$	$9.58^{+0.49}_{-0.50}$	139^{+7}_{-7}
LMC X-4	0142800101	E	$6.36^{+0.26}_{-0.11}$	$0.07^{+0.02}_{-0.03}$	597^{+171}_{-256}	-	-	-	-	-	-
LMC X-4	0142800101	OOE	-	-	-	$6.60^{+0.04}_{-0.03}$	$4.03^{+0.28}_{-0.26}$	166^{+12}_{-11}	-	-	-
LMC X-4	0203500201	OOE	$6.38^{+0.04}_{-0.04}$	$1.55^{+0.03}_{-0.03}$	117^{+2}_{-2}	-	-	-	$6.99^{+0.05}_{-0.05}$	$2.39^{+0.05}_{-0.04}$	195^{+4}_{-3}
SMC X-1	0011450101	E	$6.38^{+0.06}_{-0.06}$	$0.07^{+0.01}_{-0.01}$	126^{+18}_{-18}	-	-	-	-	-	-
SMC X-1	0011450101	OOE	-	-	-	-	-	-	-	-	-
4U 1700–377	0083280401	E	$6.37^{+0.02}_{-0.02}$	$5.96^{+0.48}_{-0.49}$	1258^{+101}_{-103}	-	-	-	-	-	-
4U 1700–377	0083280401	OOE	$6.44^{+0.06}_{-0.06}$	$14.88^{+5.55}_{-5.43}$	191^{+71}_{-70}	-	-	-	-	-	-
4U 1700–377	0600950101	E	$6.39^{+0.002}_{-0.002}$	$4.89^{+0.06}_{-0.06}$	1061^{+13}_{-13}	$6.68^{+0.05}_{-0.04}$	$0.26^{+0.05}_{-0.04}$	22^{+4}_{-3}	-	-	-
4U 1538–522	0152780201	E	$6.38^{+0.01}_{-0.01}$	$0.57^{+0.03}_{-0.03}$	792^{+42}_{-42}	$6.69^{+0.02}_{-0.02}$	$0.17^{+0.02}_{-0.02}$	145^{+17}_{-17}	$6.95^{+0.02}_{-0.02}$	$0.13^{+0.01}_{-0.01}$	181^{+14}_{-14}
4U 1538–522	0152780201	OOE	$6.42^{+0.07}_{-0.07}$	$2.46^{+0.64}_{-0.57}$	79^{+22}_{-18}	-	-	-	-	-	-
IGR J18027–2016	0745060401	E	$6.41^{+0.06}_{-0.05}$	$0.07^{+0.04}_{-0.03}$	445^{+254}_{-191}	$6.66^{+0.32}_{-0.36}$	$0.07^{+0.03}_{-0.04}$	382^{+164}_{-218}	-	-	-
IGR J18027–2016	0745060401	OOE	-	-	-	-	-	-	-	-	-
IGRJ17252–3616	0405640201	E	$6.40^{+0.03}_{-0.03}$	$0.13^{+0.02}_{-0.03}$	2695^{+415}_{-622}	-	-	-	-	-	-
IGRJ17252–3616	0405640601	E	$6.41^{+0.02}_{-0.02}$	$0.18^{+0.04}_{-0.03}$	1831^{+407}_{-305}	-	-	-	-	-	-
IGRJ17252–3616	04056401001	E	$6.40^{+0.33}_{-0.27}$	$0.04^{+0.03}_{-0.02}$	921^{+691}_{-460}	-	-	-	-	-	-
IGR J16479–4514	0512180101	E	$6.41^{+0.02}_{-0.02}$	$0.09^{+0.01}_{-0.01}$	803^{+89}_{-89}	-	-	-	$6.88^{+0.23}_{-0.12}$	$0.05^{+0.26}_{-0.18}$	576^{+345}_{-230}
IGR J16418–4532	0679810101	E	$6.43^{+0.04}_{-0.04}$	$0.06^{+0.02}_{-0.02}$	1358^{+453}_{-453}	-	-	-	$6.94^{+0.36}_{-0.27}$	$0.05^{+0.03}_{-0.02}$	1911^{+1146}_{-764}

Table 6
Ratios of out-of-eclipse to eclipse (OOE/E) fluxes in 0.3-10 keV energy range and equivalent widths of Fe emission lines

Source	Observation ID	Flux ratio (0.3-10 keV)	ratio of eqv width (Fluorescent Fe K_{α})	ratio of eqv width (Fe XXV)	ratio of eqv width (Fe XXVI)
Cen X-3	0111010101	9.79	1.82	0.53	0.66
LMC X-4	0142800101	237.18	-	-	-
LMC X-4	0203500201	86.00	-	-	-
SMC X-1	0011450101	76.62	-	-	-
4U 1700-377	0083280401	8.01	0.15	-	-
4U 1538-522	0152780201	30.28	0.1	-	-
IGR J18027-2016	0745060401	43.38	-	-	-

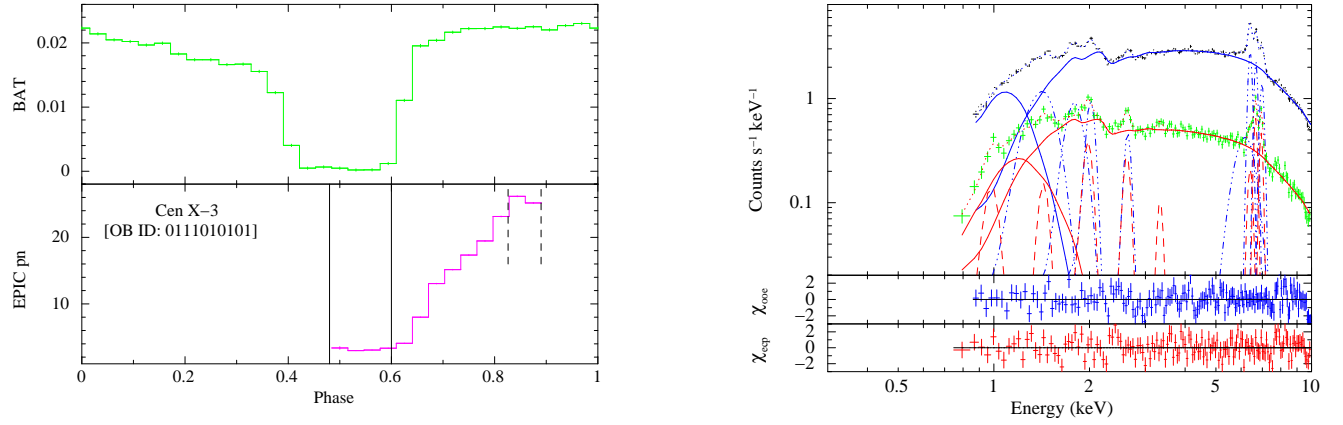


Figure 1. **Left figure:** Top panel shows the long term average BAT orbital profile of Cen X-3 and the bottom panel shows EPIC pn light curve of Cen X-3 (OB ID: 0111010101) folded with its orbital period. The eclipse spectrum and the out-of-eclipse spectrum was extracted from the duration shown with the solid and the dashed lines respectively. **Right figure:** Top Panel gives the EPIC pn out-of-eclipse and the eclipse spectrum of Cen X-3, where datapoints for the out-of-eclipse spectrum are plotted with colour black and that of eclipse spectrum are plotted with colour green. Model components of the out-of-eclipse and the eclipse spectrum is shown with the colour blue and red respectively. The emission line for the out-of-eclipse spectrum is shown with blue lines and those for the eclipse spectrum are shown with red lines. The middle and bottom panels show the contribution of each bin towards χ for the best fit spectral model for the out-of-eclipse spectrum and the eclipse spectrum respectively.

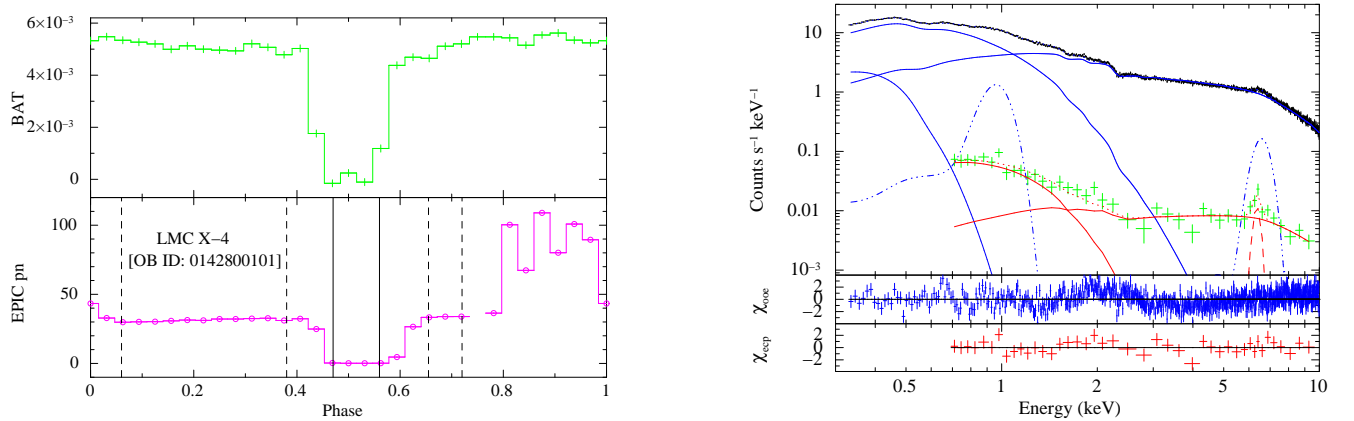


Figure 2. Same as Figure 1 for LMC X-4 (OB ID: 0142800101)

Table 7Emission line energy, flux and equivalent width other than Fe emission lines. Line fluxes are given in units of 10^{-4} photons $\text{cm}^{-2} \text{sec}^{-1}$.

Source name (OB ID)	Line energy (keV)	Phase	Emission line flux	Emission line eqv. width (eV)	Line identification	Previous detection (keV, line)
Cen X-3 (0111010101)	$0.98^{+0.01}_{-0.02}$	E	$10.5^{+5.5}_{-3.6}$	96^{+50}_{-33}	Ne X	1.022, Ne X (eclipse) ^[v1] ; 1.022, Ne X (All phase ranges) ^[v2]
	$1.43^{+0.02}_{-0.02}$	E	$0.83^{+0.27}_{-0.25}$	37^{+12}_{-11}	Mg XII	1.472, Mg XII (All phase ranges) ^[v2]
	$1.98^{+0.01}_{-0.02}$	E	$1.24^{+0.25}_{-0.20}$	102^{+20}_{-16}	Si XIV and / P $K_{\alpha 1}$, $K_{\alpha 2}$	2.00 ± 0.01 , Si XIV (eclipse) ^[v1]
	$2.62^{+0.01}_{-0.02}$	E	$0.91^{+0.15}_{-0.11}$	94^{+15}_{-11}	Cl $K_{\alpha 1}$, $K_{\alpha 2}$ and / Si XVI	2.64 ± 0.02 , Si XVI (eclipse) ^[v1] ; 2.621, S XVI (All phase ranges) ^[v2]
	$3.34^{+0.04}_{-0.04}$	E	$0.29^{+0.08}_{-0.08}$	35^{+10}_{-10}	K $K_{\alpha 1}$, $K_{\alpha 2}$	-
LMC X-4 (0142800101)	$1.34^{+0.04}_{-0.06}$	OOE	$65.47^{+24.06}_{-18.12}$	345^{+127}_{-95}	Mg $K_{\beta 1}$	-
	$1.79^{+0.03}_{-0.03}$	OOE	$12.23^{+3.27}_{-2.65}$	114^{+30}_{-25}	Si $K_{\alpha 1}$, $K_{\alpha 2}$, $K_{\beta 1}$	1.79 ± 0.05 , Si I and or Si XIII (pre-eclipse) ^[v1]
	$2.02^{+0.01}_{-0.01}$	OOE	$5.51^{+0.89}_{-1.1}$	53^{+9}_{-11}	Si XIV and / P $K_{\alpha 1}$, $K_{\alpha 2}$	1.99 ± 0.02 , Si XIV (pre-eclipse) ^[v1] ; 2.006, Si XIV (All phase ranges) ^[v2]
	$2.64^{+0.02}_{-0.02}$	OOE	$2.48^{+0.39}_{-0.40}$	29^{+5}_{-5}	Cl $K_{\alpha 1}$, $K_{\alpha 2}$ and / Si XVI	2.64 (fixed), Si XVI (pre-eclipse) ^[v1] ; 2.621, S XVI (All phase ranges) ^[v2]
	$6.19^{+0.15}_{-0.19}$	OOE	$10.41^{+2.39}_{-2.80}$	133^{+31}_{-36}	-	-
LMC X-4 (0203500201)	$0.96^{+0.01}_{-0.01}$	OOE	$7.36^{+0.05}_{-0.05}$	29^{+0}_{-0}	Cu L_{β} / Zn L_{α}	0.91434 keV (13.560 A $^{\circ}$), Ne IX He $_{\alpha}$ ^[w1] 1.01977 keV (12.158 A $^{\circ}$), Ne X Ly $_{\alpha}$ ^[w1]
4U 1700-377 (0600950101)	$0.98^{+0.03}_{-0.03}$	OOE	$5.65^{+2.02}_{-1.54}$	34^{+12}_{-9}	Cu L_{β} / Zn L_{α}	0.91434 keV (13.560 A $^{\circ}$), Ne IX He $_{\alpha}$ ^[w1] 1.01977 keV (12.158 A $^{\circ}$), Ne X Ly $_{\alpha}$ ^[w1]
4U 1700-377 (0600950101)	$0.81^{+0.10}_{-0.13}$	E	$8.11^{+32.5}_{-3.95}$	90^{+359}_{-44}	Ne K_{α} , O VIII RRC	0.86 ± 0.02 , Ne K_{α} , O VIII RRC (eclipse) ^[x1]
	$1.28^{+0.05}_{-0.05}$	E	$2.05^{+0.07}_{-0.40}$	1208^{+41}_{-236}	Mg $K_{\alpha 1}$, $K_{\alpha 2}$, $K_{\beta 1}$	1.30 ± 0.01 , Mg K_{α} , Mg XI He $_{\alpha}$ (eclipse) ^[x1]
	$1.75^{+0.01}_{-0.01}$	E	$0.87^{+0.14}_{-0.11}$	898^{+144}_{-113}	Si $K_{\alpha 1}$, $K_{\alpha 2}$ / Al XIII Ly $_{\alpha}$	1.75 ± 0.01 , Si K_{α} , Al XIII Ly $_{\alpha}$ (eclipse) ^[x1]
	$1.97^{+0.03}_{-0.03}$	E	$0.16^{+0.03}_{-0.03}$	139^{+26}_{-26}	Si XIV Ly $_{\alpha}$	2.00 ± 0.01 , Si XIV Ly $_{\alpha}$ (eclipse) ^[x1]
	$2.34^{+0.01}_{-0.01}$	E	$0.52^{+0.06}_{-0.05}$	392^{+45}_{-38}	S K_{α} , Al XIII RRC	2.33 ± 0.01 , S K_{α} , Al XIII RRC (eclipse) ^[x1]
	$2.57^{+0.05}_{-0.06}$	E	$0.08^{+0.02}_{-0.02}$	54^{+14}_{-14}	Cl $K_{\alpha 1}$, $K_{\alpha 2}$ / S XVI Ly $_{\alpha}$, Si XIV RRC	2.63 ± 0.01 , S XVI Ly $_{\alpha}$, Si XIV RRC (eclipse) ^[x1]
	$2.99^{+0.01}_{-0.01}$	E	$0.21^{+0.02}_{-0.02}$	115^{+11}_{-11}	Ar $K_{\alpha 1}$, $K_{\alpha 2}$	2.97 ± 0.01 , Ar K_{α} (eclipse) ^[x1]
	$3.70^{+0.01}_{-0.01}$	E	$0.25^{+0.03}_{-0.03}$	102^{+12}_{-12}	Ca $K_{\alpha 1}$, $K_{\alpha 2}$	3.71 ± 0.01 , Ca K_{α} (eclipse) ^[x1]
	$4.12^{+0.05}_{-0.05}$	E	$0.08^{+0.02}_{-0.02}$	29^{+7}_{-7}	Sn $L_{\gamma 1}$ / Sb $L_{\beta 2}$ / Xe L_{α} / Sc $K_{\alpha 1}$, $K_{\alpha 2}$	-
	$7.05^{+0.02}_{-0.01}$	E	$0.88^{+0.10}_{-0.13}$	219^{+25}_{-32}	Fe $K_{\beta 1}$	-
4U 1538-522 (0152780201)	$7.49^{+0.02}_{-0.02}$	E	$0.29^{+0.06}_{-0.05}$	71^{+15}_{-12}	Co $K_{\beta 1}$, Ni $K_{\alpha 1}$, $K_{\alpha 2}$	-
	$1.26^{+0.05}_{-0.07}$	E	$0.22^{+0.07}_{-0.04}$	321^{+102}_{-58}	Mg $K_{\alpha 1}$, $K_{\alpha 2}$, $K_{\beta 1}$	1.34 (fixed), Mg K_{α} , Mg XI He $_{\alpha}$ (eclipse) ^[y1]
	$1.85^{+0.03}_{-0.03}$	E	$0.15^{+0.02}_{-0.02}$	250^{+33}_{-33}	Si $K_{\beta 1}$	$1.848^{+0.012}_{0.024}$, Si XIII He $_{\alpha}$ (eclipse) ^[y1]
	$2.40^{+0.04}_{-0.03}$	E	$0.07^{+0.01}_{-0.01}$	116^{+17}_{-17}	S $K_{\beta 1}$	$2.4427^{+0.0023}_{0.023}$, S XV He $_{\alpha}$ (eclipse) ^[y1]
IGR J17252-3616 (0405640201)	$6.02^{+0.05}_{-0.05}$	E	$0.04^{+0.01}_{-0.01}$	54^{+14}_{-14}	Cr $K_{\beta 1}$	-
	$7.01^{+0.14}_{-0.40}$	E	$0.05^{+0.04}_{-0.01}$	1227^{+982}_{-245}	-	-

v1: (Ebisawa et al. 1996) v2: (Wojdowski, Liedahl & Sako 2001) w1: (Neilsen et al. 2009) x1: (van der Meer et al. 2005b) y1: (Rodes-Roca et al. 2011)

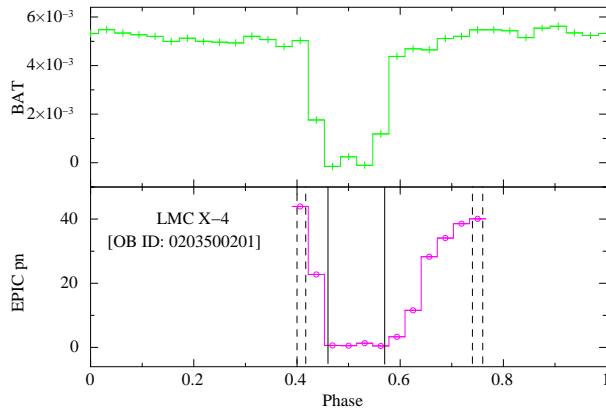


Figure 3. Same as Figure 1 for LMC X-4 (OB ID: 0203500201)

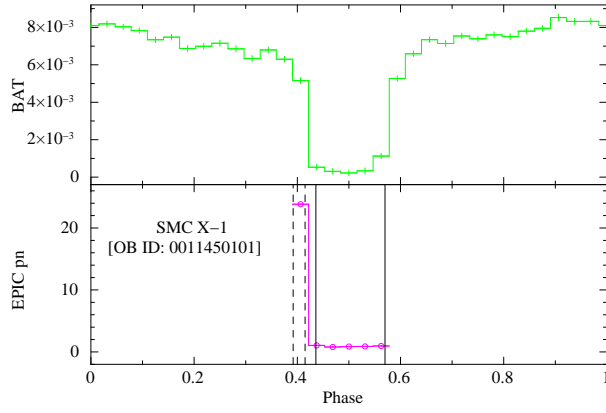
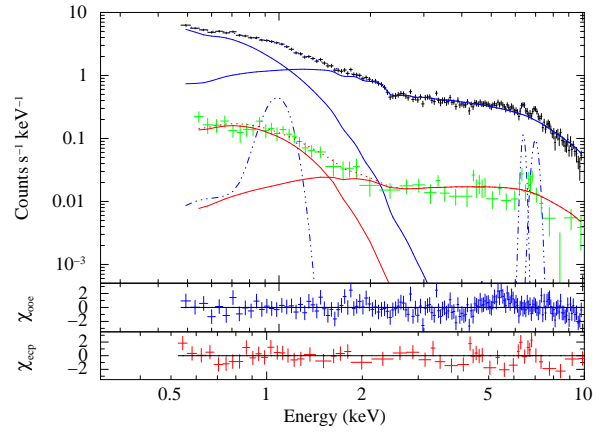


Figure 4. Same as Figure 1 for SMC X-1 (OB ID: 0011450101)

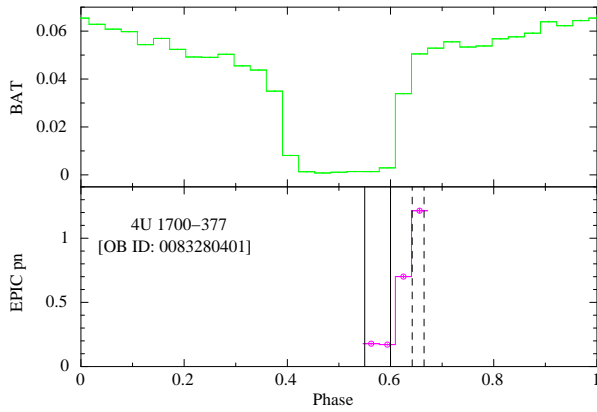
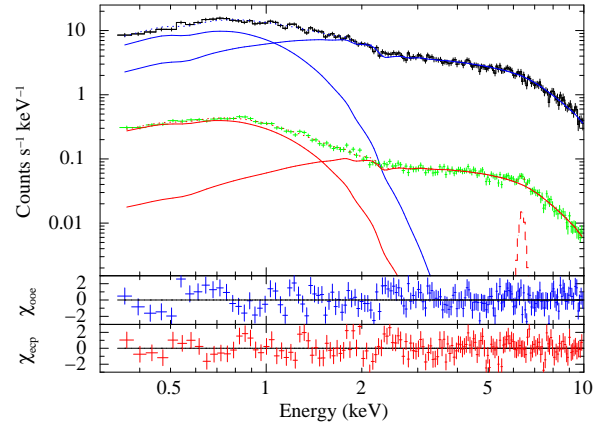
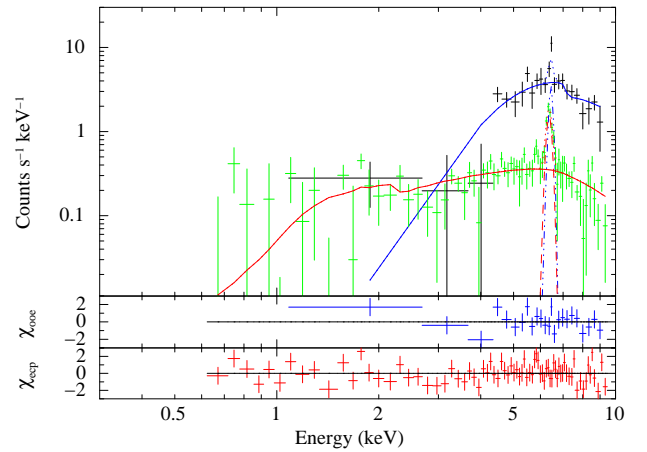


Figure 5. Same as Figure 1 for 4U 1700-377 (OB ID: 0083280401)



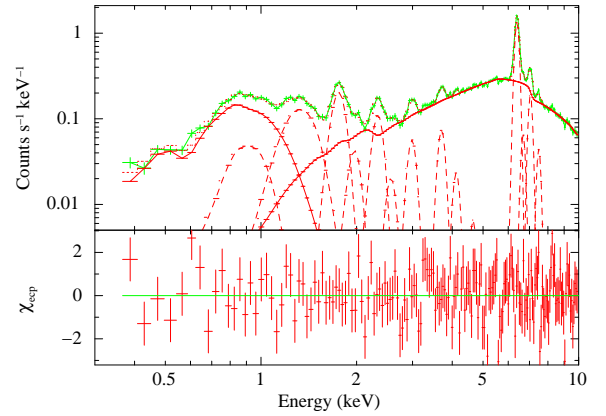
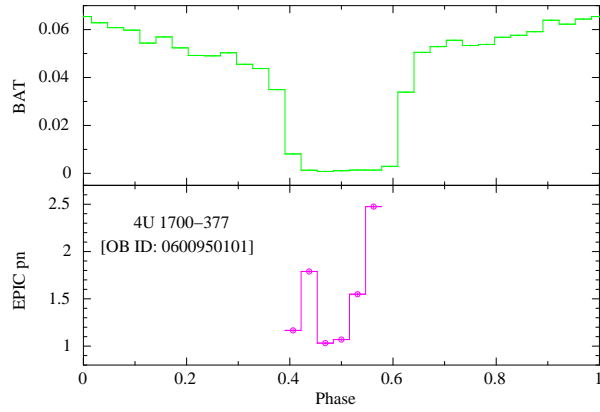


Figure 6. Left figure: Top panel shows the long term average BAT orbital profile of 4U 1700–377 and the bottom panel shows EPIC pn light curve of 4U 1700–377 (OB ID: 0600950101) folded with its orbital period. Right figure: Top Panel gives the EPIC pn eclipse spectrum of 4U 1700–377 (OB ID: 0600950101). The bottom panels show the residuals to the best fit spectral model for the eclipse spectrum.

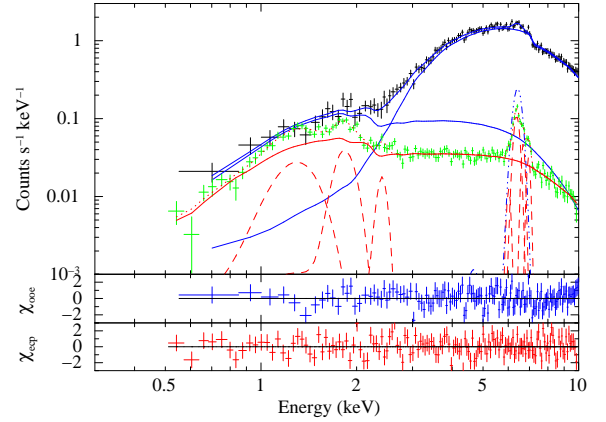
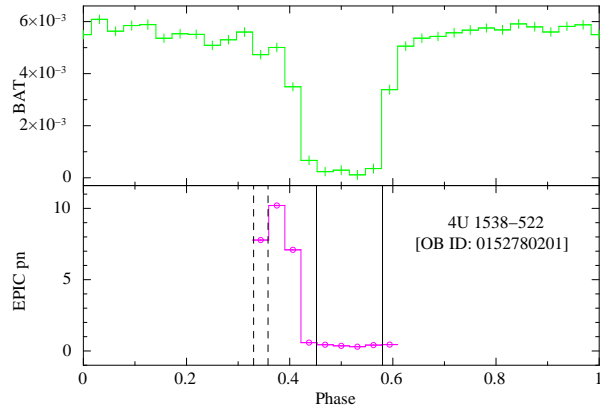


Figure 7. Same as Figure 1 for 4U 1538–522 (OB ID: 0152780201)

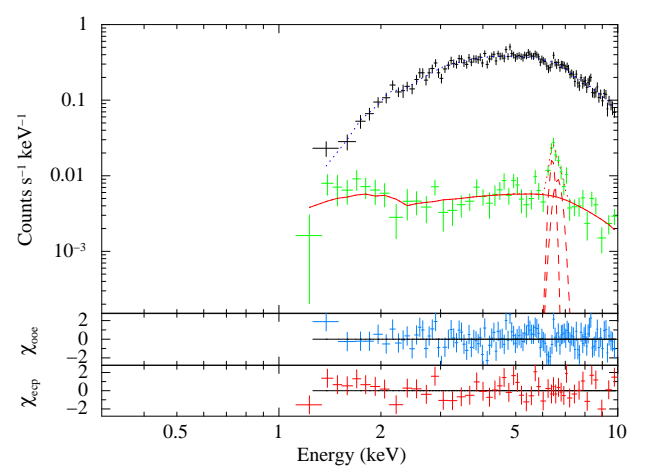
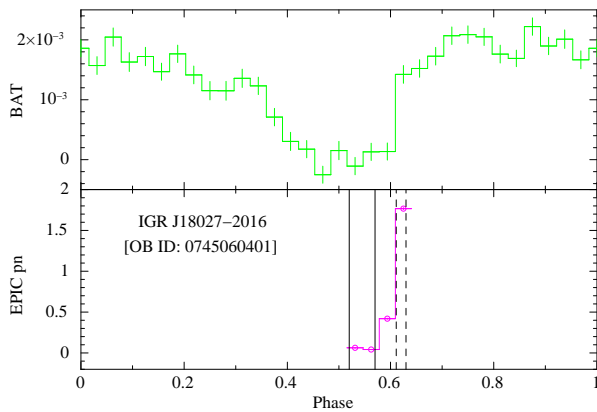


Figure 8. Same as Figure 1 for IGR J18027–2016 (OB ID: 0745060401)

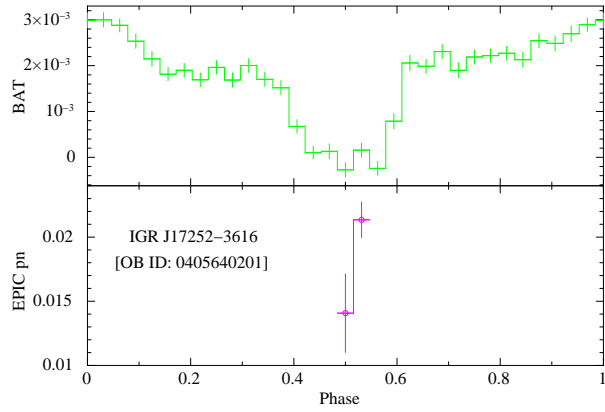


Figure 9. Same as Figure 6 for IGR J17252-3616 (OB ID: 0405640201)

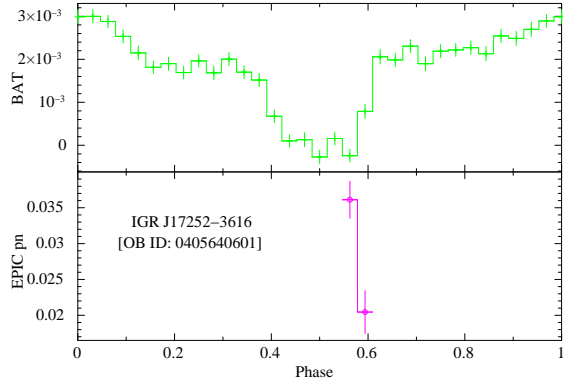
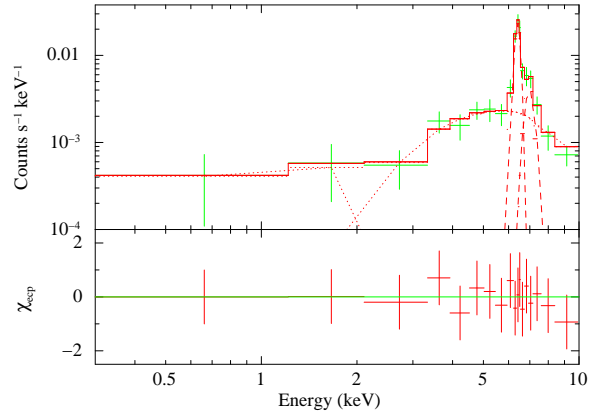


Figure 10. Same as Figure 6 for IGR J17252-3616 (OB ID: 0405640601)

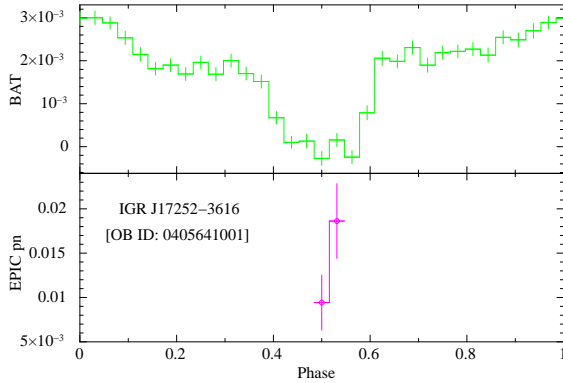
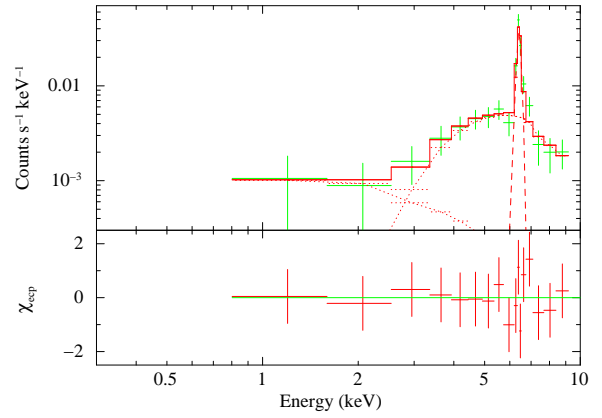
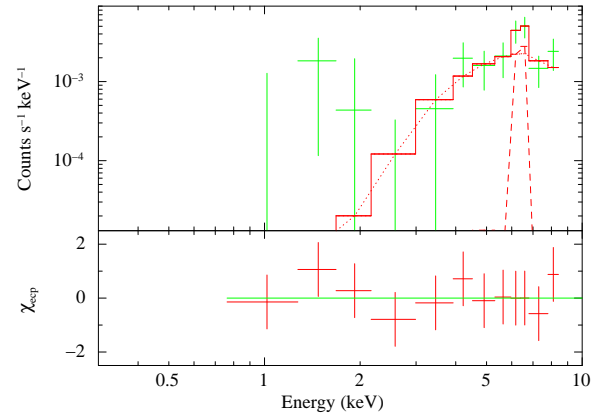


Figure 11. Same as Figure 6 for IGR J17252-3616 (OB ID: 0405641001)



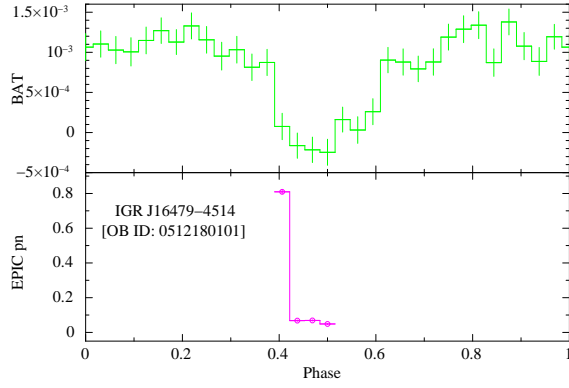


Figure 12. Same as Figure 6 for IGR J16479–4514 (OB ID: 0512180101)

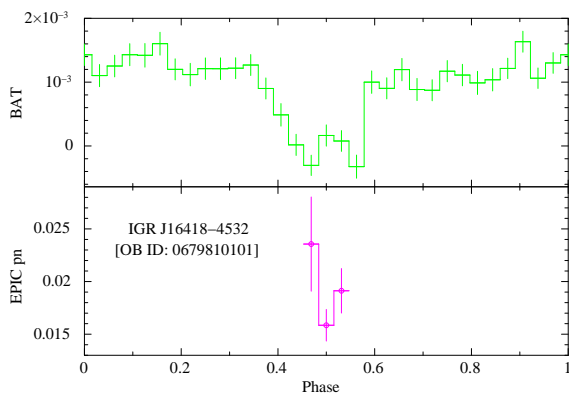
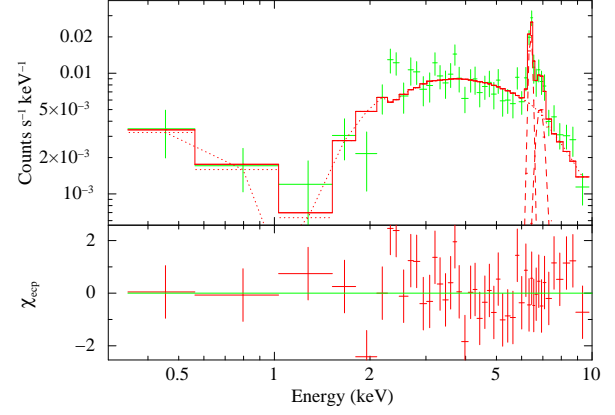
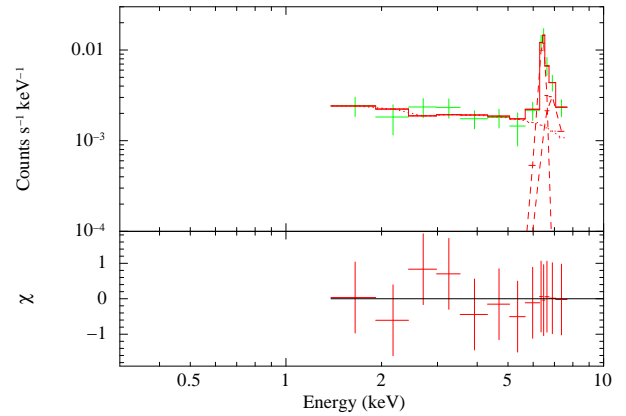


Figure 13. Same as Figure 6 for IGR J16418–4532 (OB ID: 0679810101)



REFERENCES

- Aftab N., Islam N., Paul B., 2016, *MNRAS*, 463, 2032
- Ankay A., Kaper L., de Bruijne J. H. J., Dewi J., Hoogerwerf R., Savonije G. J., 2001, *A&A*, 370, 170
- Ash T. D. C., Reynolds A. P., Roche P., Norton A. J., Still M. D., Morales-Rueda L., 1999, *MNRAS*, 307, 357
- Audley, M. D., Nagase, F., Mitsuda, K., Angelini, L., & Kelley, R. L. 2006, *MNRAS*, 367, 1147
- Augello G., Iaria R., Robba N. R., Di Salvo T., Burderi L., Lavagetto G., Stella L., 2003, *ApJL*, 596, L63
- Barthelmy S. D. et al., 2005, *Space Sci. Rev.*, 120, 143
- Becker R. H., Swank J. H., Boldt E. A., Holt S. S., Serlemitsos P. J., Pravdo S. H., Saba J. R., 1977, *ApJL*, 216, L11
- Beri A., Paul B., 2017, *New A*, 56, 94
- Bildsten L. et al., 1997, *ApJS*, 113, 367
- Blondin J. M., 1994, *ApJ*, 435, 756
- Bozzo E., Giunta A., Stella L., Falanga M., Israel G., Campana S., 2009, *A&A*, 502, 21
- Burderi, L., Di Salvo, T., Robba, N. R., La Barbera, A., & Guainazzi, M. 2000, *ApJ*, 530, 429
- Clark J. S., Goodwin S. P., Crowther P. A., Kaper L., Fairbairn M., Langer N., Brocksopp C., 2002, *A&A*, 392, 909
- Coe, M. J., Burnell, S. J. B., Engel, A. R., Evans, A. J., & Quenby, J. J. 1981, *MNRAS*, 197, 247
- Coleiro A., Chaty S., Zurita Heras J. A., Rahoui F., Tomsick J. A., 2013, *A&A*, 560, A108
- Coley J. B., Corbet R. H. D., Krimm H. A., 2015, *ApJ*, 808, 140
- Corbet R. et al., 2006, *The Astronomer's Telegram*, 779
- Corbet R. H. D., Krimm H. A., 2013, *ApJ*, 778, 45
- Day C. S. R., Stevens I. R., 1993, *ApJ*, 403, 322
- de Jong J. A., van Paradijs J., Augusteijn T., 1996, *A&A*, 314, 484
- del Sordo S., dal Fiume D., Oriandini M., Piraino S., Santangelo A., Segreto A., 2000, *Advances in Space Research*, 25, 413
- Drave S. P., Bird A. J., Goossens M. E., Sidoli L., Sguera V., Fiocchi M., Bazzano A., 2013a, *The Astronomer's Telegram*, 5131
- Drave S. P., Bird A. J., Sidoli L., Sguera V., McBride V. A., Hill A. B., Bazzano A., Goossens M. E., 2013b, *MNRAS*, 433, 528
- Ebisawa K., Day C. S. R., Kallman T. R., Nagase F., Kotani T., Kawashima K., Kitamoto S., Woo J. W., 1996, *PASJ*, 48, 425
- Falanga M., Bozzo E., Lutovinov A., Bonnet-Bidaud J. M., Fetisova Y., Puls J., 2015, *A&A*, 577, A130
- Giménez-García, A., Torrejón, J. M., Eikmann, W., et al. 2015, *A&A*, 576, A108
- Gehrels N. et al., 2004, *ApJ*, 611, 1005
- George, I. M., & Fabian, A. C. 1991, *MNRAS*, 249, 352
- Giacconi R., Gursky H., Kellogg E., Schreier E., Tananbaum H., 1971, *ApJL*, 167, L67
- Gierliński M., Done C., Page K., 2009, *MNRAS*, 392, 1106
- Haberl F., Aoki T., Mavromatakis F., 1994, *A&A*, 288, 796
- Haberl F., Day C. S. R., 1992, *A&A*, 263, 241
- Hemphill, P. B., Rothschild, R. E., Cheatham, D. M., et al. 2019, *ApJ*, 873, 62
- Hemphill, P. B., Rothschild, R. E., Markowitz, A., et al. 2014, *ApJ*, 792, 14
- Hickox, R. C., & Vrtilek, S. D. 2005, *ApJ*, 633, 1064
- Hilditch R. W., Howarth I. D., Harries T. J., 2005, *MNRAS*, 357, 304
- Hill A. B. et al., 2005, *A&A*, 439, 255
- Hu C.-P., Chou Y., Yang T.-C., Su Y.-H., 2013, *ApJ*, 773, 58
- Hung, L.-W., Baniados, E., De Propriis, R., & West, M. J. 2010, *ApJ*, 720, 1483
- in't Zand J. J. M., 2005, *A&A*, 441, L1
- Islam N., Paul B., 2014, *MNRAS*, 441, 2539
- Islam N., Paul B., 2016, *MNRAS*, 461, 816
- Jain C., Paul B., Dutta A., 2009a, *MNRAS*, 397, L11
- Jain C., Paul B., Dutta A., 2009b, *Research in Astronomy and Astrophysics*, 9, 1303
- Jaisawal G. K., Naik S., 2015, *MNRAS*, 448, 620
- Jethwa P. 2012, *Pile-up thresholds for the EPIC cameras*, 1, 4
- Jones C., Forman W., Tananbaum H., Schreier E., Gursky H., Kellogg E., Giacconi R., 1973, *ApJL*, 181, L43
- Kaastra, J. S., & Mewe, R. 1993, *A&AS*, 97, 443
- Kirsch M. G. F. et al., 2006, *A&A*, 453, 173
- Krimm H. A. et al., 2013a, *ApJS*, 209, 14
- Krimm H. A. et al., 2013b, *ApJS*, 209, 14
- Kubota, M., Odaka, H., Tamagawa, T., & Nakano, T. 2018, *ApJL*, 868, L26
- Lang F. L. et al., 1981, *ApJL*, 246, L21
- Levine A., Rappaport S., Deeter J. E., Boynton P. E., Nagase F., 1993, *ApJ*, 410, 328
- Levine A. M., Rappaport S. A., Zojcheski G., 2000, *ApJ*, 541, 194
- Li F., Rappaport S., Epstein A., 1978, *Nature*, 271, 37
- Liu Q. Z., van Paradijs J., van den Heuvel E. P. J., 2000, *A&AS*, 147, 25
- Lumb D. H., Scharfel N., Jansen F. A., 2012, *ArXiv e-prints*
- Lutovinov, A. A., Tsygankov, S. S., Postnov, K. A., et al. 2017, *MNRAS*, 466, 593
- Maccarone T. J., Girard T. M., Casetti-Dinescu D. I., 2014, *MNRAS*, 440, 1626
- Manousakis A., Walter R., 2011, *A&A*, 526, A62
- Martínez-Núñez S. et al., 2017, *Space Sci. Rev.*, 212, 59
- Martins F., Schaerer D., Hillier D. J., 2005, *A&A*, 436, 1049
- Mason K. O. et al., 2001, *A&A*, 365, L36
- Molkov S., Mowlavi N., Goldwurm A., Strong A., Lund N., Paul J., Oosterbroek T., 2003, *The Astronomer's Telegram*, 176
- Moon D.-S., Eikenberry S. S., Wasserman I. M., 2003, *ApJ*, 586, 1280
- Mukherjee U., Raichur H., Paul B., Naik S., Bhatt N., 2006, *Journal of Astrophysics and Astronomy*, 27, 411
- Nagase F., Corbet R. H. D., Day C. S. R., Inoue H., Takeshima T., Yoshida K., Mihara T., 1992, *ApJ*, 396, 147
- Naik S., Paul B., 2004a, *A&A*, 418, 655
- Naik S., Paul B., 2004b, *ApJ*, 600, 351
- Naik S., Paul B., 2012, *Bulletin of the Astronomical Society of India*, 40, 503
- Naik S., Paul B., Ali Z., 2011, *ApJ*, 737, 79
- Negueruela I., Smith D. M., Reig P., Chaty S., Torrejón J. M., 2006, in *ESA Special Publication*, Vol. 604, *The X-ray Universe 2005*, Wilson A., ed., p. 165
- Neilsen J., Lee J. C., Nowak M. A., Dennerl K., Vrtilek S. D., 2009, *ApJ*, 696, 182
- Nespoli E., Fabregat J., Mennickent R. E., 2008, *A&A*, 486, 911
- Oskinova L. M., Feldmeier A., Kretschmar P., 2013, in *IAU Symposium*, Vol. 290, *IAU Symposium*, Zhang C. M., Belloni T., Méndez M., Zhang S. N., eds., pp. 287–288
- Parkes G. E., Murdin P. G., Mason K. O., 1978, *MNRAS*, 184, 73P
- Paul B., Kitamoto S., 2002, *Journal of Astrophysics and Astronomy*, 23, 33
- Penny A. J., Olowin R. P., Penfold J. E., Warren P. R., 1973, *MNRAS*, 163, 7P
- Pietrzyński G. et al., 2013, *Nature*, 495, 76
- Pike, S. N., Harrison, F. A., Bachetti, M., et al. 2019, *ApJ*, 875, 144
- Pradhan P., Bozzo E., Paul B., 2018, *A&A*, 610, A50
- Price, R. E., Groves D. J., Rodrigues, R. M., Seward, F. D., Swift, C. D. & Toor, ApJ, 168, L7
- Primini F., Rappaport S., Joss P. C., 1977, *ApJ*, 217, 543
- Raichur H., Paul B., 2010, *MNRAS*, 401, 1532
- Reynolds A. P., Bell S. A., Hilditch R. W., 1992, *MNRAS*, 256, 631
- Reynolds A. P., Hilditch R. W., Bell S. A., Hill G., 1993, *MNRAS*, 261, 337
- Robba, N. R., Burderi, L., Di Salvo, T., Iaria, R., & Cusumano, G. 2001, *ApJ*, 562, 950
- Rodes-Roca J. J., Page K. L., Torrejón J. M., Osborne J. P., Bernabéu G., 2011, *A&A*, 526, A64
- Romano P. et al., 2012, *MNRAS*, 419, 2695
- Romano P. et al., 2011, *The Astronomer's Telegram*, 3174
- Romano P. et al., 2009, *MNRAS*, 399, 2021
- Romano P. et al., 2008, *ApJL*, 680, L137
- Sako, M., Liedahl, D. A., Kahn, S. M., & Paerels, F. 1999, *ApJ*, 525, 921
- Santangelo, A., del Sordo, S., Segreto, A., et al. 1998, *A&A*, 340, L55
- Savonije G. J., 1978, *A&A*, 62, 317
- Schreier E., Giacconi R., Gursky H., Kellogg E., Tananbaum H., 1972a, *ApJL*, 178, L71
- Schreier E., Levinson R., Gursky H., Kellogg E., Tananbaum H., Giacconi R., 1972b, *ApJL*, 172, L79
- Schulz, N. S., Canizares, C. R., Lee, J. C., & Sako, M. 2002, *ApJL*, 564, L21
- Sguera V. et al., 2005, *A&A*, 444, 221
- Shtykovsky, A. E., Arefiev, V. A., Lutovinov, A. A., & Molkov, S. V. 2018, *Astronomy Letters*, 44, 149
- Sidoli L. et al., 2012a, in *Proceedings of "An INTEGRAL view of the high-energy sky (the first 10 years)" - 9th INTEGRAL Workshop and celebration of the 10th anniversary of the launch (INTEGRAL 2012). 15-19 October 2012. Bibliothèque Nationale de France, Paris, France. Published online at <http://pos.sissa.it/cgi-bin/reader/conf.cgi?confid=176> & http://pos.sissa.it/cgi-bin/reader/conf.cgi?confid=176/A_i, id.34, p. 34*
- Sidoli L. et al., 2013, *MNRAS*, 429, 2763
- Sidoli L., Mereghetti S., Sguera V., Pizzolato F., 2012b, *MNRAS*, 420, 554
- Sidoli L. et al., 2008, *ApJ*, 687, 1230
- Strüder L. et al., 2001, *A&A*, 365, L18
- Suleimanov V., Meyer F., Meyer-Hofmeister E., 2003, *A&A*, 401, 1009
- Takeuchi Y., Koyama K., Warwick R. S., 1990, *PASJ*, 42, 287
- Tawara Y., Yamauchi S., Awaki H., Kii T., Koyama K., Nagase F., 1989, *PASJ*, 41, 473
- Thompson T. W. J., Rothschild R. E., 2009, *ApJ*, 691, 1744

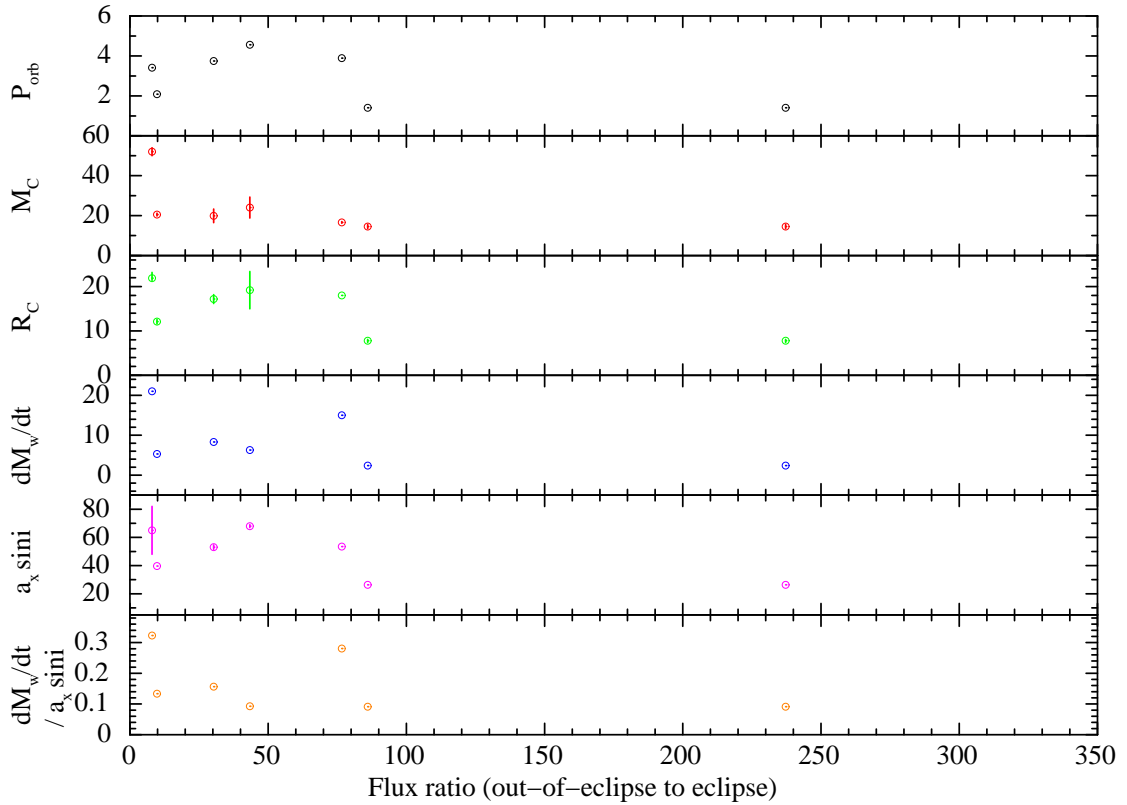


Figure 14. Plot of different orbital parameters of the eclipsing HMXBs with out-of-eclipse to eclipse flux ratios. P_{orb} : Orbital Period (days), M_C : Mass of the companion (M_{\odot}), R_C : Radius of the companion star (R_{\odot}), \dot{M}_w : Mass loss rate of the companion star ($10^{-7} M_{\odot} \text{ yr}^{-1}$), $a_x \text{ sini}$: Projected length of the semi major axis of the system in the plane along the line of sight (light-sec). M_{\odot} , R_{\odot} : Mass and radius of Sun respectively.

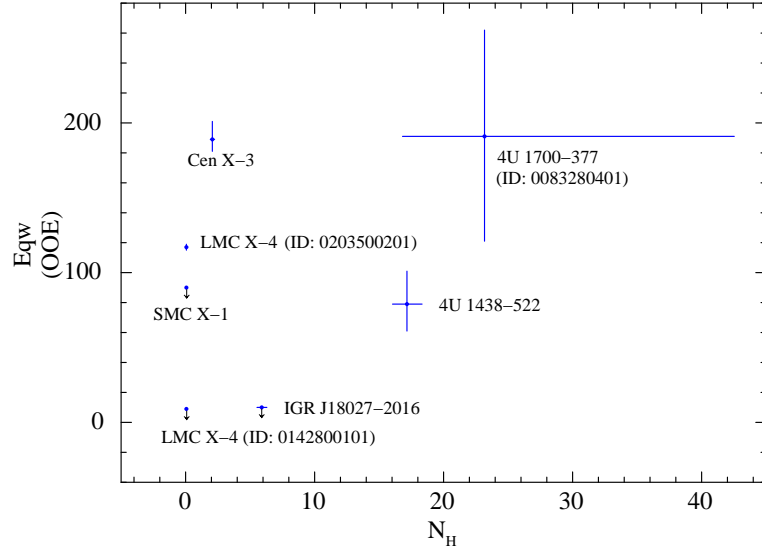


Figure 15. Equivalent width (E_{qw} , along Y axis) vs. line of sight equivalent Hydrogen column density (N_H , along X axis) of fluorescent Fe K_{α} emission line in out-of-eclipse (OOE) phase. This line is detected in Cen X-3, LMC X-4 (ID: 0203500201), 4U 1700-477 (ID: 0083280401) and in 4U 1538-522, whereas upper limit of equivalent width is shown in SMC X-1, LMC X-4 (ID: 0142800101) and IGR J18027-2016. Unfortunately one can not correlate the relationship between N_H and equivalent width of fluorescent Fe K_{α} emission line in this sample of SgHMXBs due to the limitation of the available data.

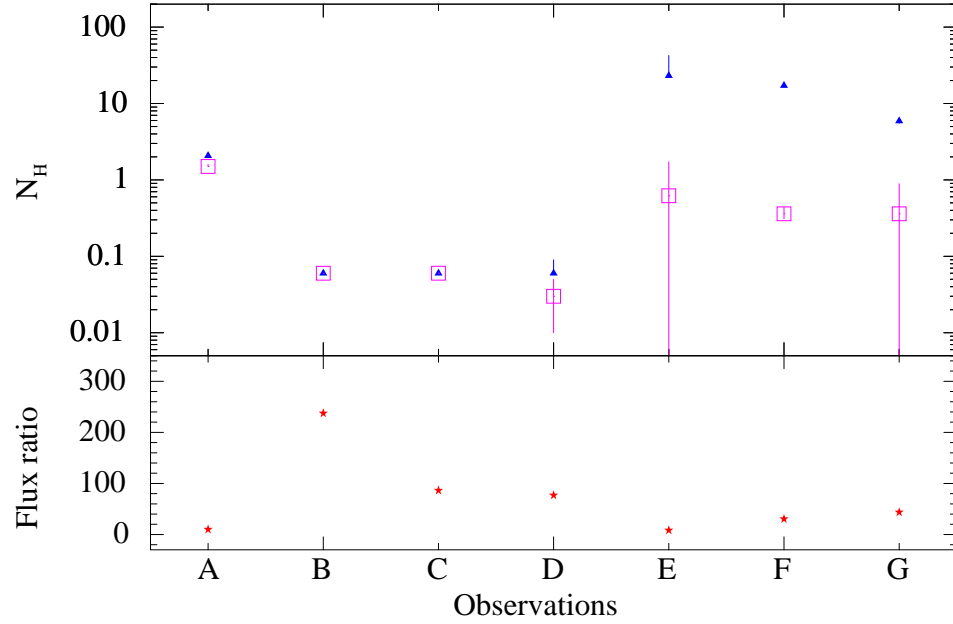


Figure 16. Line of sight equivalent Hydrogen column density (N_H) of HMXBs during eclipse and out-of-eclipse phase for observations having data for both the phases. X axis gives the observations and the Y axis in the top panel shows N_H (eclipse: pink boxes, out-of-eclipse: blue triangles). Y axis in the bottom panel gives the value of 0.3-10 keV out-of-eclipse to eclipse flux ratio. A: Cen X-3, B: LMC X-4 OB ID: 0142800101, C: LMC X-4 OB ID: 0203500201, D: SMC X-1, E: 4U 1700-377 OB ID: 0083280401, F: 4U 1538-522, G: IGR J18027-2016. For 3 observations (4U 1700-377 OB ID: 0083280401, 4U 1538-522, IGR J18027-2016) N_H is larger during eclipse than out-of-eclipse phase. For the other 4 observations N_H is comparable in both the phases.

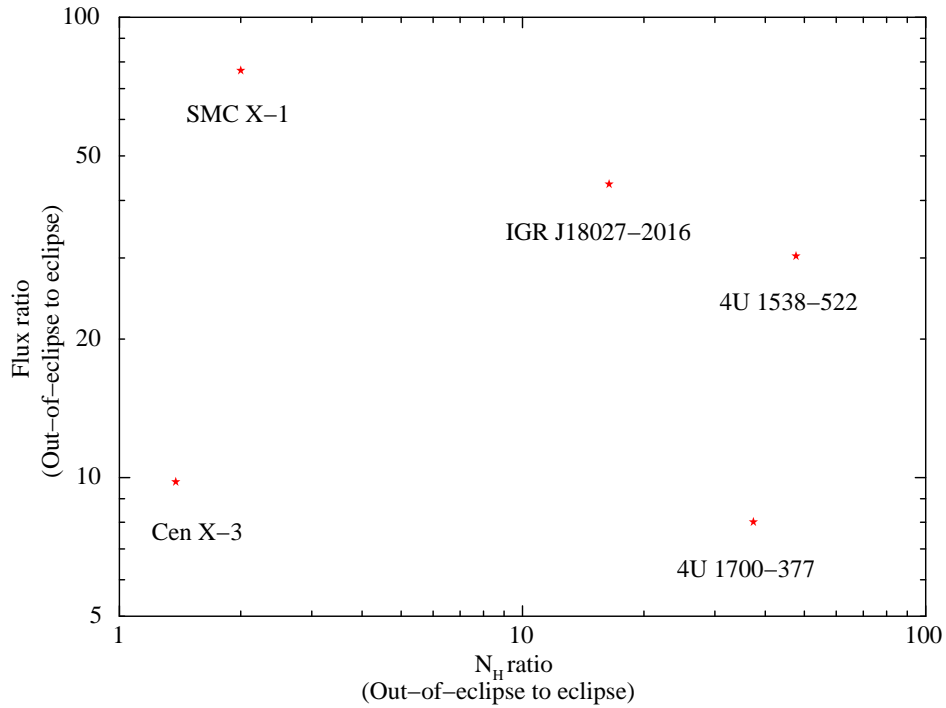


Figure 17. Variation of out-of-eclipse to eclipse flux ratio with corresponding ratio of the line of sight equivalent Hydrogen column density (N_H) of HMXBs. X axis shows the out-of-eclipse to eclipse ratio of N_H and Y axis gives the out-of-eclipse to eclipse flux ratio. Here the observation of 4U 1700-377 belongs to OB ID: 0083280401

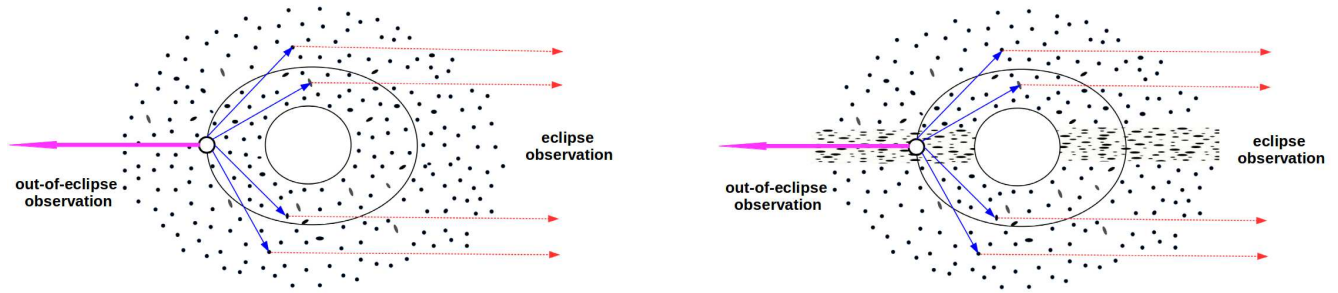


Figure 18. A probable distribution of wind around the neutron star in systems with low ratio of the column density (N_H) in the out-of-eclipse to eclipse phase (left) and in systems in which this ratio of column densities is much larger (right). The small circle at the left of each Figure represents the neutron star and the bigger one represents the companion star. The primary and reprocessed X-rays are represented with solid and dashed arrows respectively. The first system probably have more isotropic wind pattern. A strong wind outflow in the equatorial or near equatorial plane in the second system can explain the higher ratio of column densities between the out-of-eclipse to eclipse phase. During eclipse, the reprocessed X-rays represented with the dashed arrows reach the observer and in both the systems it shows comparable N_H . When the source is in out-of-eclipse phase the observer receives the direct X-rays, shown here with bold (pink) arrows. In case of the first systems during out-of-eclipse phase, the observer looks through an isotropic wind as seen during eclipse. But for the second system during out-of-eclipse phase, the direct X-rays reach the observer penetrating dense wind.

- Thompson T. W. J., Tomsick J. A., in 't Zand J. J. M., Rothschild R. E., Walter R., 2007, *ApJ*, 661, 447
 Torrejón J. M., Negueruela I., Smith D. M., Harrison T. E., 2010, *A&A*, 510, A61
 Torrejón, J. M., Schulz, N. S., Nowak, M. A., & Kallman, T. R. 2010, *ApJ*, 715, 947
 Turner M. J. L. et al., 2001, *A&A*, 365, L27
 Ulmer, M. P., Baity, W. A., Wheaton, W. A., & Peterson, L. E. 1973, *Nature Physical Science*, 242, 121
 Vacca W. D., Garmany C. D., Shull J. M., 1996, *ApJ*, 460, 914
 Val Baker A. K. F., Norton A. J., Quaintrell H., 2005, *A&A*, 441, 685
 van der Meer A., Kaper L., di Salvo T., Méndez M., van der Klis M., Barr P., Trams N. R., 2005a, *A&A*, 432, 999
 van der Meer A., Kaper L., di Salvo T., Méndez M., van der Klis M., Barr P., Trams N. R., 2005b, *A&A*, 432, 999
 van der Meer A., Kaper L., van Kerkwijk M. H., Heemskerk M. H. M., van den Heuvel E. P. J., 2007, *A&A*, 473, 523
 Varun, Maitra C., Pradhan, P., Raichur H., & Paul B. 2019, *MNRAS*, 484, L1
 Walter R. et al., 2004, *The Astronomer's Telegram*, 229
 Walter R., Zurita Heras J., 2007, *A&A*, 476, 335
 Walter R. et al., 2006, *A&A*, 453, 133
 Weaver K. A., Nousek J., Yaqoob T., Mushotzky R. F., Makino F., Otani C., 1996, *ApJ*, 458, 160
 White N. E., 1978, *Nature*, 271, 38
 White N. E., Kallman T. R., Swank J. H., 1983, *ApJ*, 269, 264
 Wojdowski P., Clark G. W., Levine A. M., Woo J. W., Zhang S. N., 1998, *ApJ*, 502, 253
 Wojdowski P. S., Liedahl D. A., Sako M., 2001, *ApJ*, 547, 973
 Woo J. W., Clark G. W., Levine A. M., Corbet R. H. D., Nagase F., 1996, *ApJ*, 467, 811
 Zurita Heras J. A., De Cesare G., Walter R., Bodaghee A., Bélanger G., Courvoisier T. J.-L., Shaw S. E., Stephen J. B., 2006, *A&A*, 448, 261
 Zycki P. T., Krolik J. H., Zdziarski A. A., Kallman T. R., 1994, *ApJ*, 437, 597